



KTH Engineering Sciences

Structure formation, phase transitions and drag interactions  
in multicomponent superconductors and superfluids

KARL SELLIN

Doctoral thesis in theoretical physics  
Stockholm, Sweden 2018

TRITA-FYS 2017:78  
ISSN 0280-316X  
ISRN KTH/FYS/--17:78-SE  
ISBN 978-91-7729-657-7

Institutionen för fysik, KTH  
AlbaNova universitetscentrum  
SE-106 91 Stockholm Sweden

Akademisk avhandling som med tillstånd av Kungl Tekniska högskolan  
framlägges till offentlig granskning för avläggande av teknologie doktorsex-  
amen i fysik med inriktning teoretisk fysik 9 februari 2018 kl 14:00 i sal  
FB42, AlbaNova Universitetscentrum.

© Karl Sellin, February 2018

Tryck: Universitetsservice US AB

## Sammanfattning

Supraledning och suprafluiditet är några av de mest grundläggande och viktiga fenomenen i modern fysik. Dock har mycket av det teoretiska arbetet för sådana system hittills varit begränsat till enkomponentfallet. För flerkomponentsystem kan spektrat av möjliga topologiska defekter, deras strukturformationer och därtill relaterade fasövergångar, alla vara mycket rikare än i enkomponentfallet, vilket motiverar teoretiska studier av flerkomponentsystem.

I denna avhandling diskuteras strukturformationer av virvlar med komplicerade växelverkningar på grund av flerkomponenteffekter med hjälp av Monte-Carlo-punkt-partikel-simuleringar. Förutom de triangulära gitter som förekommer för typ-2-supraledande virvlar i enkomponentfallet, visas det att en rik mängd strukturella faser är möjliga för virvlar i flerkomponentsystem.

Eftersom virvlar spelar en nyckelroll i fasövergångar, studeras även problemet med fasövergångar i flerkomponentsystem i denna avhandling. Givet ett Peskin-Dasgupta-Halperin dualitetsargument för enkomponentfallet hade det var naturligt att tro att  $U(1)$  gitter-London-supraleddare endast kan ha en kontinuerlig inverterad-XY fasövergång. Det diskuteras här att den icke-triviala interna strukturen hos virvlar i flerkomponents- $U(1)$ -London-supraledare kan istället leda till en första ordningens fasövergång, något som stöds av storskaliga Monte-Carlo-simuleringar. Även för sådana system, för vilka virvellinjer är axiellt symmetriska i grundtillståndet, kan en termiskt framkallad splittring av kompositvirvlar till fraktionella virvlar leda till en fasseparation av virvellinjer, vilket i sin tur resulterar i en första ordningens supraledande fasövergång.

En liknande fasseparation kan förekomma för tvåkomponent-supraledare på grund av en Andreev-Bashkin drag-växelverkan, för vilken en fasseparation kan förekomma även i grundtillståndet: draget kan orsaka att kompositvirvlar sönderfaller till attraktivt växelverkande skyrmioner. En sådan drag-växelverkan kan ha omfattande konsekvenser när det gäller fasövergångar, rotationell respons och virvelstrukturer i flerkomponentsystem. Denna avhandling avslutas sålunda med mikroskopiska beräkningar av en sådan Andreev-Bashkin drag-växelverkan i en generaliserad Bose-Hubbard-modell av tvåartsbosoner i ett optisk gitter, med mask-kvant-Monte-Carlo-simuleringar. Beroenden mellan drag-växelverkan och boson-boson-växelverkan samt egenskaperna hos det optiska gittret karakteriseras, och *ihopkopplade faser* (där endast sam- eller mot-flöde sker) observeras.

## **Abstract**

Superconductivity and superfluidity are some of the most fundamental and important phenomena of modern physics. However, much theoretical work for such systems so far has been restricted to the one-component case. For multicomponent systems, the spectrum of possible topological defects, their structure formation and associated phase transitions, can all be much richer than in the one-component case, motivating theoretical studies of multicomponent systems.

In this thesis, the structure formation of vortices with complicated interactions due to multicomponent effects are considered using point-particle Monte Carlo simulations. Besides the triangular vortex lattices found for one-component type-2 superconducting vortices, it is found that a rich plethora of structural phases is possible for vortices in multicomponent systems.

Since vortices play a key role in phase transitions, the problem of phase transitions in multicomponent systems is also studied in this thesis. It could be expected that  $U(1)$  lattice London superconductors can only have a continuous “inverted-XY” phase transition by a Peskin-Dasgupta-Halperin duality argument for the one-component case. It is discussed here that the non-trivial internal structure of vortices in multicomponent  $U(1)$  London superconductors can instead lead to a first-order phase transition, which is supported by large-scale parallel tempering Monte Carlo simulations. Even for such systems, where in the ground state vortex lines are axially symmetric, thermally induced splitting of composite vortices into fractional vortices can lead to a phase separation of vortex tangles, rendering the superconducting phase transition first-order.

A similar phase separation can occur for two-component superconductors with an Andreev-Bashkin drag interaction, for which a phase separation can occur even in the ground state: the drag can cause composite vortices to decay into attractively interacting skyrmions. Such drag interactions can to a large extent influence phase transitions, rotational response and vortex structures in multicomponent systems. This thesis thus finishes with microscopic calculations of such an Andreev-Bashkin drag interaction in an extended Bose-Hubbard model of two-species bosons in an optical lattice, using worm quantum Monte Carlo simulations. Dependencies of the drag interaction on boson-boson interactions and properties of the optical lattice are characterized, and paired phases (where only co- or counter-flow states occur) are observed.

# Acknowledgements

This thesis is the result of the 879 processor years used from resources provided by the Swedish National Infrastructure for Computing (SNIC) at the National Supercomputer Center in Linköping, Sweden.

First of all, thanks to my advisor Egor Babaev for his ideas, knowledge, feedback and continuing support. I have enjoyed his many entertaining stories and cultural observations and I am very grateful for being given the chance to do physics research. Thanks to Mats Wallin and Jack Lidmar for many useful computational physics discussions. Thanks also to Edwin Langmann, Anatoly Belonoshko and Patrik Henelius for whom I've been a teaching assistant, for sharing their insights. Thanks to Olle Edholm for running and mountain discussion. Thanks to all of the above for being nice people in general.

Many thanks to the fellow PhD and master students (past and present) for many entertaining discussions. I will miss the daily lunch break which typically begins with expert analysis of current news events and ends in a passionate whiteboard discussion. In no particular order and hoping not to forget anyone thanks to Linnea, Mikael, David, Farrokh, Jie, Stella, Hannes, Richard, Richard, Per, Oskar, Juan Carlos, Faezeh. Thanks also to Daniel, Julien, Mihail, Thomas and Johan, past and present office mates and group members, as well as Filipp and Emil who recently joined the office, and are outcompeting everyone with their benchpress skills.

Of course, in particular thanks to my parents for support and care, without which life would have been very difficult. Many thanks also to aunt Birgitta for being an extra Stockholm parent. Thanks to sister Maja with Andreas, and I guess thanks to Sten and the unborn child also, who I hope will find this thesis to be of great interest. Many thanks to the rest of friends and family up in Norrland, who have supported me despite that I left paradise to study physics in Stockholm. Of course, thanks to my friend and cousin Viktor for many fond memories for the duration of our lives, especially for our many deep discussions in the sauna. Thanks also to Mattias and Johan for their friendship and great taste in beer and in music respectively.

Thanks also to new friends and family I have down in Stockholm be-

cause of Hanna. One-component systems are not as much fun as multi-component, as the reader of this thesis will certainly become aware, so I am happy to form a rich and interesting two-component system with Hanna. Especially thanks to her of course, for laughing hard at my jokes from the first day. Her company is something I greatly treasure.

# Contents

<b>Contents</b>	<b>7</b>
<b>I Background and selected results</b>	<b>1</b>
<b>1 Superconductivity and superfluidity: a brief overview</b>	<b>3</b>
1.1 Superconductivity . . . . .	4
1.2 Vortices and different types of superconductors . . . . .	4
1.3 The order of the superconducting phase transition . . . . .	8
1.4 Superfluidity . . . . .	9
<b>2 Statistical physics and Monte Carlo methods</b>	<b>11</b>
2.1 Averages in statistical physics . . . . .	11
2.2 Monte Carlo integration . . . . .	12
2.3 The Metropolis Monte Carlo method . . . . .	13
2.4 Finite-size scaling and parallel tempering . . . . .	14
2.5 Phase transitions: definition and classification . . . . .	15
<b>3 Vortex structure formation</b>	<b>17</b>
3.1 Hierarchical structure formation . . . . .	18
3.2 Stripe phases due to non-pairwise interaction . . . . .	18
3.3 Vortices with dipolar forces . . . . .	18
<b>4 Phase transitions in multicomponent London superconductors</b>	<b>31</b>
4.1 Two-component London superconductivity . . . . .	31
4.2 Derivation of the Josephson length $\xi_J$ . . . . .	32
4.3 Discretization of the two-component London free energy . . . . .	33
4.4 Two-component lattice London superconductivity . . . . .	35
<b>5 Drag interaction in the two-species Bose-Hubbard model</b>	<b>41</b>
5.1 The Bose-Hubbard model . . . . .	42
5.2 Quantum Monte Carlo for the BH model . . . . .	49
5.3 Worm algorithm for the BH model . . . . .	51

5.4 Two-component Bose-Hubbard model and calculated drag interaction . . . . .	58
<b>6 Conclusions and outlook</b>	<b>61</b>
<b>Bibliography</b>	<b>65</b>
<b>II Scientific Papers</b>	<b>81</b>

## **Part I**

# **Background and selected results**



## **Chapter 1**

# **Superconductivity and superfluidity: a brief overview**

In this chapter a brief overview of superconductivity and superfluidity is given, with emphasis on aspects such as vortices and their associated structure formation and phase transitions. *Quantum vortices* are of crucial importance for understanding superfluid and superconducting systems, as was realized by Onsager [1], Feynman [2] and Abrikosov [3]. Furthermore, the work by Berezinskii [4], Kosterlitz and Thouless [5] suggested that an unusual phase transition can occur due to a thermally activated proliferation of vortices, a phenomenon that is a display of a fundamental connection between topological defects and phase transitions. These important works, and much of the theoretical work on superfluidity and superconductivity so far, have considered systems with *one* component. However, the one-component case is only a special case of the general *multicomponent* case.

In multicomponent systems there is a rich spectrum of possible topological defects, for example: knot solitons [6], vortices with fractional flux [7] and skyrmions [8]. The physics of multicomponent systems is therefore rich, since vortices and topological defects to a large extent influence the physics of superfluids and superconductors. Apart from triangular vortex lattices found for one-component type-2 superconducting vortices, there are many possible structure formations of topological defects in multicomponent systems, for example: *square* vortex lattices [9] and semi-Meissner states [10]. Phase transitions can also be entirely different in multicomponent systems. An important phase transition is the continuous  $\lambda$ -transition observed in e.g. liquid helium [11]. Onsager suggested that vortex loops are the cause for disorder in the superfluid  $\lambda$ -transition [12], later Peskin [13] proposed a duality between a three-dimensional lattice superfluid model and a corresponding lattice London superconductor model,

which was backed by Monte Carlo simulations by Dasgupta and Halperin [14]. In multicomponent systems, the phase transition can be first-order even for systems for which a one-component counterpart should display a  $\lambda$ -type continuous phase transition, as has been found with Monte Carlo simulations [15, 16, 17, 18].

## 1.1 Superconductivity

Key properties of superconducting materials are the vanishing of electrical resistivity [19] and magnetic fields [20] (the Meissner effect). The heat capacity of aluminum for low temperatures is shown in Fig. 1.1 a). For low temperatures in Fig. 1.1 a), the material is in a superconducting state and the heat capacity depends sub-linearly with temperature, a key property to reproduce theoretically [21]. This feature, and others, were reproduced with BCS-theory [22], see Fig. 1.1 a). For our purposes, the Ginzburg-Landau (GL) theory [23] is more useful. GL theory was formulated before the BCS-theory and has been derived from BCS-theory close to the critical temperature [24]. In GL theory, and in the one-component case, a complex order parameter field  $\psi$  determines the free-energy density

$$f = \alpha|\psi|^2 + \frac{1}{2}\beta|\psi|^4 + \frac{1}{2}|(\nabla + ieA)\psi|^2 + \frac{1}{2}(\nabla \times A)^2, \quad (1.1)$$

where the coefficients  $\alpha$  and  $\beta$  may depend on temperature,  $A$  is the magnetic vector potential and  $e$  the charge coupling. Writing  $\psi = |\psi|e^{i\theta}$ , it can be noted that this theory has a local  $U(1)$ -symmetry, since (1.1) is invariant under the transformations  $\theta \rightarrow \theta + \phi$ ,  $A \rightarrow A - \nabla\phi/e$ , where  $\phi$  is a spatially dependent single-valued function. It can also be noted that two characteristic length scales are contained in this theory, the magnetic penetration depth  $\lambda$  and the coherence length  $\xi$  [25], corresponding to the decay of the magnetic field in a Meissner domain and the correlation of the order parameter field respectively. The limit of constant density  $|\psi|$  but varying phase  $\theta$  is referred to as the *London limit* and will be used extensively in this thesis.

## 1.2 Vortices and different types of superconductors

Abrikosov [3] found that when superconductors with  $\kappa \equiv \lambda/\xi > 1/\sqrt{2} \approx 0.71$  are in a sufficiently strong applied magnetic field, the field can penetrate the sample with spatial periodicity. At the points of magnetic maximum, the order parameter vanishes and following a contour around such a point causes the phase to wind by  $2\pi$ . This state is called the *vortex state*. Superconductors have therefore been sorted into two types, those with at-

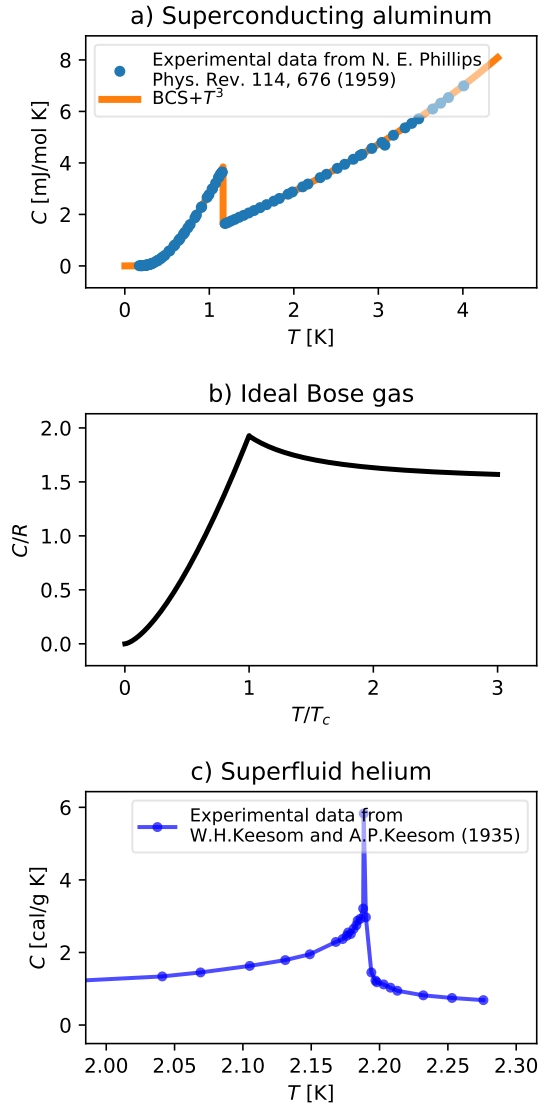


**Figure 1.1:** Plots of heat capacities for a) a superconductor b) a Bose-Einstein condensate c) a superfluid. In a) experimental superconducting aluminum measurements tabulated in Ref. [26] is shown together with BCS theory heat capacity [22] where a phonon  $T^3$  contribution has been added. In b) the theoretical heat capacity of an ideal gas of bosons in a box in the thermodynamic limit is shown, see [27]. In c) the superfluid  $\lambda$ -transition for helium-4 under vapor pressure is shown with data from experimental measurements tabulated in Ref. [11].

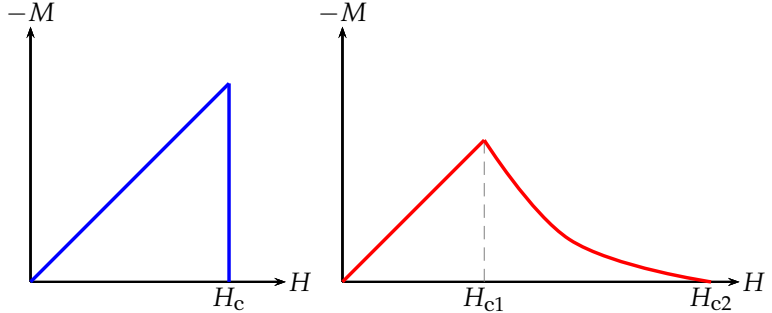


**Figure 1.2:** Schematic behavior of the magnetization  $M$  in type-1 (left) and type-2 (right) superconductors, in an applied magnetic field  $H$ .

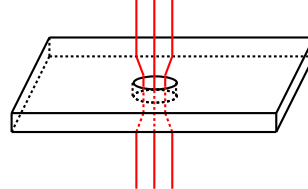


**Figure 1.3:** Illustration of a vortex in a superconducting slab which allows magnetic field lines (red) to penetrate.

tractively interacting vortices (type-1:  $\kappa < 1/\sqrt{2}$ ) and those with repulsively interacting vortices (type-2:  $\kappa > 1/\sqrt{2}$ ) [25].

In the Meissner state an external magnetic field  $H$  is canceled by the magnetization  $M$ . However, this screening is only possible up to a critical point, see Fig. 1.2. For type-1 superconductors, there is a single critical field  $H_c$ , and the superconductor is in its Meissner state for  $H < H_c$  and in its normal state for  $H > H_c$ . For type-2 superconductors there are two critical fields,  $H_{c1}$  and  $H_{c2}$ , where  $H < H_{c1}$  is the Meissner state,  $H_{c1} < H < H_{c2}$  is the vortex state ( $H_{c1}$  corresponds to the entrance of the first vortex), and  $H > H_{c2}$  is the normal state. In the vortex state magnetic flux tubes penetrate the superconductor as illustrated in Fig. 1.3 and can minimize a mutual repulsion energy by forming a triangular lattice.

In recent years it has been shown that multicomponent superconductors can have length scales such that they are not classifiable as type-1 nor as type-2 [10]. For a two-component superconductor which has two coherence lengths  $\xi_1$  and  $\xi_2$  and with  $\kappa_i = \lambda/\xi_i$ , the case with  $\kappa_1 < 1/\sqrt{2}$  and  $\kappa_2 > 1/\sqrt{2}$  was given the name type-1.5 superconductivity [29] and generated further theoretical and experimental activity [30, 31, 32, 33, 34, 35, 36, 37, 38, 39]. In such systems the pairwise interactions between

vortices can be short-range repulsive and long-range attractive, which can lead to vortex clustering and a ‘semi-Meissner’ state, where regions of a sample are in a vortex state, and other regions are in a Meissner state. Such systems may also have strong non-pairwise interactions due to the non-linearity of the theory, which can create complicated filamentary vortex structures [34, 40, 41]. Vortex matter in type-1.5 superconductors may also form vortex cluster glass states in clean systems [42].

Vortices are also fundamentally important for the study of phase transitions of many systems, one famous example being the Berezinskii-Kosterlitz-Thouless (BKT) transition. For low-dimensional systems with  $d < 3$ , it was shown [43] that there is no continuous symmetry breaking for finite temperature in systems with short-range interactions (the Mermin-Wagner theorem). Consider the XY-model with continuous  $U(1)$  symmetry given by

$$H = -J \sum_{i\mu} \cos(\theta_{i+\hat{\mu}} - \theta_i), \quad (1.2)$$

where  $i$  is a site index and  $J > 0$  is a coupling strength. For the 2DXY we have  $\mu = x, y$  so that  $\hat{\mu} = \hat{x}, \hat{y}$ , and the sum  $\sum_{i\mu}$  goes over nearest neighbors on a two-dimensional square lattice, where periodic boundary conditions are usually assumed. It was thought that this model in two dimensions, for which the Mermin-Wagner theorem applies, has no symmetry breaking and thus no phase transition. It was nevertheless shown that a kind of transition between an ordered and a disordered phase can occur due to vortex proliferation [4, 5]. The fact a proliferation of vortices can lead to a transition can be understood from a simple energy-entropy balance argument for a system of a single vortex situated somewhere on a 2D lattice of size  $L^2$  with lattice spacing  $a$ . The energy density is then  $(\nabla\theta)^2/2$  with  $\theta = \varphi$ , giving the total energy (let  $J = 1$ )

$$E_v = \int dS (\nabla\theta)^2/2 = \int_a^L d\rho 2\pi\rho(1/\rho^2)/2 = \pi \ln(L/a). \quad (1.3)$$

The entropy can be estimated from the ability to place the vortex on  $(L/a)^2$  different sites, so that there are  $(L/a)^2$  microstates giving the entropy  $S = 2\ln(L/a)$ . The free energy of a system with a single vortex is in this case  $F_v = E - TS = (\pi - 2T) \ln(L/a)$  and the ground state free-energy  $F_0 = 0$  giving

$$F_v - F_0 = (\pi - 2T) \ln(L/a). \quad (1.4)$$

The system may therefore lower its free energy by introducing a vortex if  $(\pi - 2T) < 0$ , suggesting that a vortex proliferation could occur at a temperature  $T = \pi/2$ .

For a renormalization-group approach to this phenomena, see [44]. For two-dimensional superconductors, a vortex-antivortex unbinding pic-

ture is discussed in [45]. The BKT transition has been supported experimentally in studies of e.g. thin superfluid and superconducting films [46, 47, 48].

In 3D, the story of a vortex-driven phase transition is similar, however there the vortices are much more complicated as they form loops. This idea was suggested by Onsager for the  $\lambda$ -transition [12], and the scenario is sometimes called a *vortex-loop blowout* [49, 50], see also [51]. A duality mapping by Peskin [13] and subsequent Monte Carlo simulations by Dasgupta and Halperin [14] furthermore suggest that the 3DXY model is dual to a 3D lattice London superconductor, in turn suggesting that the vortex-loop blowout scenario is relevant also for superconductors in 3D.

### 1.3 The order of the superconducting phase transition

We previously noted a local  $U(1)$ -symmetry in the Ginzburg-Landau free energy (1.1) and have discussed the BKT transition that occurs in the globally  $U(1)$ -symmetric 2DXY-model. We now turn to the superconducting phase transition. In early heat capacity measurements, see Fig. 1.1 and [52], a discontinuity at the superconducting critical point was observed as well as an exponential behavior for low temperatures. BCS-theory [22] successfully reproduced both of these features, suggesting that the superconducting phase transition is of second order. However, the mean-field result from BCS theory does not account for contributions from thermally induced vortex excitations.

Fluctuations in the gauge field in the Ginzburg-Landau theory can cause the phase transition to be first-order for very type-1 superconductors ( $\kappa \ll 1/\sqrt{2}$ ) [53]. The calculations in [54] suggested that the phase transition is first-order for very type-1 superconductors, and continuous for very type-2 superconductors, with a tricritical point at  $0.8/\sqrt{2}$ , slightly below the value of  $\kappa = 1/\sqrt{2}$  separating type-1 and type-2 superconductors. A tricritical point is indeed found by Monte Carlo [55] and renormalization group [56] calculations. The value  $(0.76 \pm 0.04)/\sqrt{2}$  was found in Monte Carlo simulation [57] and a recent renormalization group study [58] found an algebraic expression  $(\sqrt{31} - \sqrt{461}/25)/\sqrt{2} = 0.62/\sqrt{2}$  (the same authors later considered the  $N$ -component case [59]).

Extending (1.2) to 3D gives the 3DXY-model which describes the continuous superfluid  $\lambda$ -transition [60, 61, 62] (to be discussed further below). The 3DXY-model is furthermore dual to the lattice London superconductor [13, 50, 51]

$$H = \sum_{i\mu} \left[ -J \cos(\theta_{i+\hat{\mu}} - \theta_i - A_{i\mu}) + \frac{1}{2} \lambda^2 [\Delta \times A]_{i\mu}^2 \right], \quad (1.5)$$

where the second term in the bracket is a discrete curl. When mapping the 3DXY-model to the lattice London superconductor the temperature axis is reversed and the London superconductor is thus said to be in the *inverted* 3DXY universality class, which was confirmed with Monte Carlo calculation [14]. See also [63, 64, 65, 66] as well as chapter 4 for further numerical studies of lattice London superconductivity.

The order of the superconducting phase transition may be different in multicomponent cases. A  $U(1) \times U(1)$ -superconductor can have a first-order phase transition [15, 16, 17, 18]. The first-order phase transition can be interpreted as an effect of the intercomponent vortex interactions and Monte Carlo calculations for effective 3D vortex-loop models with non-monotonic interactions of the type-1.5 kind can indeed demonstrate a first-order phase transition [67]. Paper 4 of this thesis considers the order of the phase transition of a two-component lattice London model where the  $U(1) \times U(1)$ -symmetry has been broken to a local  $U(1)$ -symmetry by an intercomponent phase coupling term.

## 1.4 Superfluidity

When liquid helium-4 is cooled to low enough temperatures, it can undergo a phase transition into a state characterized by zero viscosity, infinite heat conductivity and a display of the fountain and mechanocaloric effects [27, 68, 69], a *superfluid* state. The heat capacity curve for the superfluid phase transition of Fig. 1.1 c) resembles a  $\lambda$  why it is called the  $\lambda$ -transition. The specific heat of helium has been measured in microgravity with subnanokelvin temperature resolution close to the transition [62].

Superfluidity was early suggested to have some connection to Bose-Einstein condensation [70], helium-4 atoms have spin zero and are thus bosons. In Fig. 1.1 b), the heat capacity for an ideal gas of bosons is shown, showing a peak at a critical temperature, below which the bosons form a Bose-Einstein condensate. For the Bose-Einstein condensation phase transition the heat capacity has a discontinuous derivative, so it is a third order phase transition (when put in an harmonic oscillator, the transition becomes second order [71, 72, 73, 28]). A microscopic theory for the  $\lambda$ -transition was proposed by Feynman [74] during the development of the path-integral method. In this approach, the quantum statistical partition function for a  $d$ -dimensional system is mapped onto *worldlines* in a  $d+1$  dimensional space, where the extra dimension is *imaginary time* (this will be discussed further in chapter 5).

The original path-integral calculations for helium-4 were made using various approximations and showed the existence of a transition, but of third order [74]. With more computing power, the path integrals could in-

stead be sampled numerically using Monte Carlo integration [75, 76]. In such simulations the heat capacity appears to fall on a  $\lambda$ -curve. The appearance of superfluid order in the path-integral picture was put on firmer ground in the 1980s [77] using a formula relating the superfluid density to the fluctuations of the *winding number*, which is a global topological quantity of a path-integral configuration (not to be confused with the winding number associated with vortices). The winding number is the net number of times particles wind across a spatial direction when varying the ‘imaginary time’ from 0 to  $\beta$ . In the 1990s the efficiency of the path integral Monte Carlo technique was improved with the worm algorithm [78, 79], which will be described in detail in later chapters. Originally the worm algorithm was developed for space-discretized models but since then it has also been developed for continuous-space models [80, 81]. These topics will be further discussed in chapter 5.

Superfluids are, as superconductors, in general multicomponent systems, and as such much current research of superfluids consider multicomponent cases. In chapter 5 and in paper 5, multicomponent superfluids are considered and in particular an intercomponent *drag* effect is discussed.

## Chapter 2

# Statistical physics and Monte Carlo methods

Since this thesis relies on the principles of equilibrium statistical physics and Monte Carlo methods, these topics are briefly outlined in this chapter.

### 2.1 Averages in statistical physics

In equilibrium statistical physics, the properties of physical systems are understood by computing and analyzing expectation values of an observable  $O = O[\{\theta_i\}]$  where  $\{\theta_i\}$  denotes the degrees of freedom of the system. Given a Hamiltonian  $H = H[\{\theta_i\}]$  the ensemble average of  $O$  is given by

$$\langle O \rangle = \frac{1}{Z} \text{Tr} [O e^{-\beta H}], \quad (2.1)$$

where  $\beta = 1/T$  ( $k_B = 1$ ),  $Z = \text{Tr} [e^{-\beta H}]$  is the partition function, and  $\text{Tr} = \int d\{\theta_i\}$  is the trace operator which consists of integration (and/or summation) over the range of values the degrees of freedom takes.

Exact solutions [82] are rare, and otherwise the strategy has historically been to look for approximations which ease the mathematical complexity of the integrals while still preserving the essential physics. However, with computers came the possibility of numerically computing of expressions like (2.1) [83]. Since the trace operation in (2.1) amounts to high dimensional integration for any realistic system, straightforward integration by numerical discretization may very well not be a feasible strategy. Another strategy is Monte Carlo integration techniques. Monte Carlo techniques are quite practical, but also has a principal advantage of being an exact method in the sense that there is not necessarily any numerical discretization involved. Also, convergence towards the correct answer is in principle guaranteed [84].

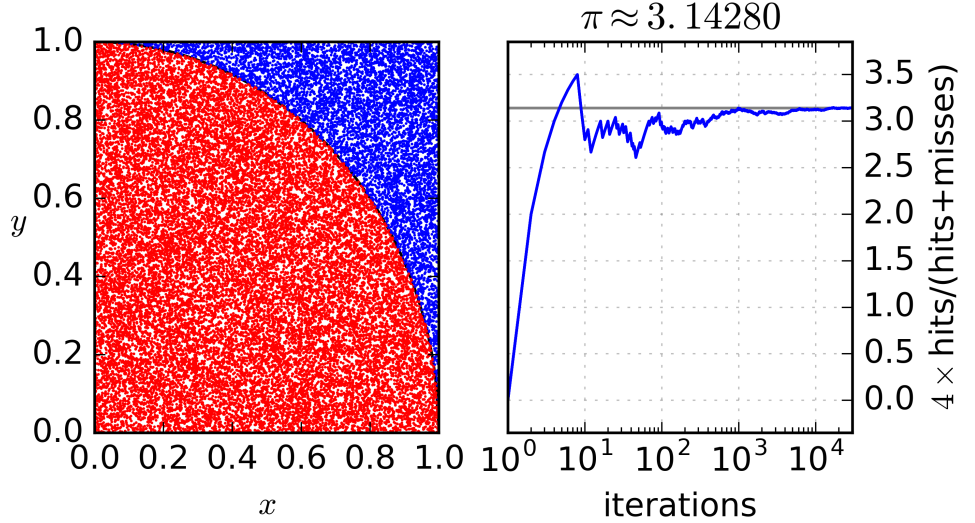


**Figure 2.1:** Calculation of  $\pi$  with random numbers, illustrating the principle of Monte Carlo integration. Red dots are hits and blue misses.

## 2.2 Monte Carlo integration

Monte Carlo methods rely on random numbers. A classic and visual example of straightforward Monte Carlo integration is the ‘hit-and-miss’ calculation of the integral  $\int_0^1 dx \sqrt{1 - x^2} = \pi/4$ , i.e. the area of a quarter unit circle. Such a calculation consists of repeated generation of sets of two random numbers  $x$  and  $y$  between zero and one, and if  $y < \sqrt{1 - x^2}$  the iteration counts as a hit. The ratio of the number of hits to the total number of iterations will tend to the area under the curve  $y = \sqrt{1 - x^2}$  and thus the integral. The method is exact in the sense that there is no discretization of the domain, and convergence is guaranteed by the law of large numbers [84]. For illustration, a realization of such a calculation is presented in Fig. 2.1 where a pseudo-random number generator was used. A similar calculation [85] obtained the value  $\pi \approx 3.131$  with a shotgun as a random number generator.

The hit-and-miss method can be naturally extended to integrals with higher dimensionality. For example, in the case of a system with degrees of freedom  $\{\theta_i\}_{i=1}^N$  we can calculate the integral

$$Z = \int d\{\theta_i\} e^{-\beta H[\{\theta_i\}]} \quad (2.2)$$

(where we denote by  $\int d\{\theta_i\}$  the integration of the range of values the de-

grees of freedom take) by generating random configurations  $\{\theta_i\}_{i=1}^N$ , and generating a random number within the range of the integrand, and counting the number of hits and misses. Note however that in the example of Fig. 2.1 there is no substantial difference between the sizes of the areas under and above the curve. If one were to compute an integral with a big such difference, the straightforward hit-and-miss method would not work well in practice as most of the iterations would be either hits or misses and the convergence would thus be slow. This is resolved by importance sampling (as opposed to the ‘simple sampling’ used in Fig. 2.1), where the contributing terms are drawn from a non-uniform distribution. For details, we refer to [84, 86, 87]. An importance sampling method which we use here is the Metropolis method.

### 2.3 The Metropolis Monte Carlo method

The principle of importance sampling in statistical physics as suggested by Metropolis et al. [83] is as follows. In Fig. 2.1 we generated numbers  $x$  and  $y$  from a uniform distribution. In the evaluation of something like (2.1), we could instead imagine generating the configurations  $\mu \equiv \{\theta_i\}_{i=1}^N$  not uniformly, but in such a way that the number of hits and misses are roughly equal. The estimated expectation value after  $M$  generated configurations  $\mu_n$  can be written

$$\langle O \rangle \approx \frac{\sum_{n=1}^M O_{\mu_n} e^{-\beta H_{\mu_n}}}{\sum_{n=1}^M e^{-\beta H_{\mu_n}}} \text{ for states } \mu_n \text{ generated with uniform probability.} \quad (2.3)$$

If we instead were to draw configurations with probabilities according to their Boltzmann weights, the estimator is simply an unweighted arithmetic average

$$\langle O \rangle \approx \frac{1}{M} \sum_{n=1}^M O_{\mu_n} \text{ for states } \mu_n \text{ generated with probability } e^{-\beta H_{\mu_n}}. \quad (2.4)$$

The remaining question is then how one generates configurations with probability according to their Boltzmann weights.

In practice, the importance sampling discussed above is obtained with a Markov chain through the Metropolis method [83]. Metropolis Monte Carlo works by proposing a new configuration  $j$  from an old configuration  $i$  with a proposal distribution  $g(i \rightarrow j)$ , which is accepted with a specified probability  $A(i \rightarrow j) = \min(1, e^{-\beta \Delta E})$  where  $\Delta E = E_j - E_i$ . Consider the time evolution of the probability of being in state  $i$ ,

$$\frac{dp_i}{dt} = \sum_j [p_j P(j \rightarrow i) - p_i P(i \rightarrow j)], \quad (2.5)$$

where  $P(i \rightarrow j)$  is the probability of transitioning from  $i$  to  $j$ . The first and second terms on the right-hand side correspond to the rate of transitioning into and out of the state  $i$  respectively. In equilibrium the time derivative is zero and (2.5) is fulfilled if (but not only if)

$$p_j P(j \rightarrow i) = p_i P(i \rightarrow j). \quad (2.6)$$

The condition of (2.6) is called *detailed balance* and is a sufficient but not necessary condition for Metropolis Monte Carlo given that states are generated ergodically, see [84, 88]. Ergodicity means that each state is reachable from every other state in a finite time, however a non-ergodic calculation may still yield useful information within an ergodic class [84].

In a simulation, the probability of transitioning from  $i$  to  $j$  is the product of the proposal and acceptance probabilities, that is  $P(i \rightarrow j) = g(i \rightarrow j)A(i \rightarrow j)$  which after insertion into the balance equation (2.6) gives

$$\frac{p_i}{p_j} = \frac{g(j \rightarrow i) \min(1, e^{-\beta(E_i - E_j)})}{g(i \rightarrow j) \min(1, e^{-\beta(E_j - E_i)})} = \frac{e^{-\beta E_i}}{e^{-\beta E_j}}, \quad (2.7)$$

assuming that the proposal distribution is symmetric. The Metropolis Monte Carlo method thus generates a chain of configurations where each configuration appears with a probability proportional to its Boltzmann weight.

The estimation of thermal averages can thus be done via arithmetic averaging of the form (2.4) by starting with some initial configuration  $\mu_0$  and generating a chain  $\mu_1, \dots, \mu_M$  via the Metropolis scheme<sup>1</sup>.

## 2.4 Finite-size scaling and parallel tempering

At first glance the computational principles outlined above may seem straightforward, but there is in practice a range of difficulties that arise when computing averages with the Metropolis method. Here a few that are relevant for this thesis will be briefly discussed.

For numerical studies of finite-size systems one can calculate the same quantities for various system sizes and then extrapolate to the thermodynamic limit. For example, scaling of thermodynamic variables like the maximum of the heat capacity and behavior of the energy histogram can determine whether a phase transition is first-order or not [89, 90, 91]. A finite size scaling analysis consists of performing simulations of different system sizes but with otherwise identical systems, and determining the dependence of various quantities on the system size. This dependence is

---

<sup>1</sup>There are two practical caveats to this: i) if the initial state  $\mu_0$  is not an equilibrium state the system must be equilibrated before sampling occurs and ii) sampling should be done with uncorrelated samples. See [86] for a reference of how Monte Carlo works in practice.

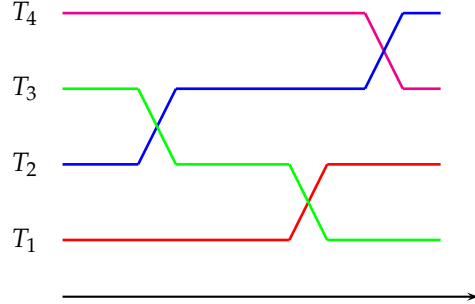


**Figure 2.2:** Illustration of parallel tempering where several replicas of a system are evolved rightwards for different temperatures  $T_1, T_2, \dots$  and exchange of such replicas are possible (illustrated by crossing lines).

then extrapolated to the thermodynamic limit. There is however no guarantee that the measured scaling holds for system sizes larger than what is accessible to numerics.

Since the Metropolis Monte Carlo method is a Markov chain, the generated configurations will be correlated. Such correlations can be quantified in terms of a characteristic correlation time [86], which can be taken as a safe sampling frequency in order to sample uncorrelated data. However, close to critical points the correlation time can diverge, which is called *critical slowing down*. There are various model-specific algorithms that circumvent this via global updates. Using the *parallel tempering* algorithm [92] is another strategy.

With parallel tempering, systems with different temperatures are simulated in parallel for a range of temperatures, as illustrated in Fig. 2.2. Each processor performs ordinary Monte Carlo updates and to this is added the trial move of swapping systems between temperatures, which can lead to reduced correlations between states [92] and that the system can ‘tunnel’ out of metastable states, as low-temperature configurations can diffuse to high-temperature simulations where energy barriers are overcome by thermal fluctuations. For strict detailed balance to be satisfied the swap moves should occur at random, but for reasons of computational efficiency the swap moves can be attempted with fixed frequency which satisfies the balance condition [88, 93].

## 2.5 Phase transitions: definition and classification

The thermodynamical bulk free-energy density  $f = \beta^{-1} \ln(Z)/V$  depends on the coupling parameters of the Hamiltonian, and thermodynamic functions are calculated via differentiation of the free energy. Such thermo-

dynamic functions may exhibit discontinuities at certain sets of coupling parameters, for which the free energy is not analytic. Such sets can be taken as definitions of phase boundaries which separate phases (i.e. regions of analyticity). The crossing of a phase boundary is then understood as a phase transition. It should be noted that the definition in terms of analytic free-energy is not completely general, considering the BKT-transition. For further details of mathematical aspects of phase transitions, we refer to [94] and for a more physical discussion to [95].

By the Ehrenfest classification [96] phase transitions are classified by the order of the derivative of the free energy which has a discontinuity at the critical point. If a first order derivative (e.g. entropy, internal energy) is discontinuous, then the phase transition is of first order. If a second order derivative (e.g. heat capacity) is discontinuous, the phase transition is of second order, and so on. The phase transitions of different order may furthermore be grouped into different types depending on the behavior of higher order derivatives, see [97]. The Ehrenfest classification is however discouraged [95, 98], for example there may be divergences rather than discontinuities in thermodynamic functions (as for the 2D Ising model without external field, where the heat capacity diverges logarithmically at  $T_c$ ). See [99] for a historical assessment of the terminology and classification of phase transitions. The modern classification of phase transitions is binary where a phase transition is either ‘first-order’ (there is a latent heat for a temperature-driven transition) or ‘continuous’ (no latent heat) [98, 95].

## **Chapter 3**

### **Vortex structure formation**

The triangular Abrikosov vortex lattice has been detected experimentally for various compounds and with various experimental techniques, see e.g. [100, 101, 102, 103]. However, more recent measurements have displayed complex vortex structures with vortex stripes, clusters and voids [29, 30, 38, 104, 105]. Although effects of *vortex pinning* may certainly be important for understanding such results, so may effects of vortex interactions more complicated than purely repulsive or attractive. A recent proposal [106] of using vortex arrays as a magnetic lattice for ultracold atom experiments and atomic quantum simulators, further motivate studies of vortex structure formation as it could provide increased experimental control of the magnetic lattice [107].

One theoretical approach to vortex structure formation is to introduce vortices into a domain and numerically minimize the free energy in a GL theory, see for example [34]. Another approach, which will be used here, is to assume forms of vortex interactions found elsewhere [34, 40] and considering vortices to be point-particles in two dimensions. The properties of a system of such point-particles can be determined with Monte Carlo methods or molecular dynamics simulations (for vortex molecular dynamics type simulations, see e.g. [107, 108, 109, 110]).

In section 3.1 paper 1 is discussed as well as results of hierarchical structure formation that were not included in the paper. In section 3.2 we discuss paper 2, which describes stripe phases that arise due to non-pairwise interactions. In section 3.3 we discuss paper 3 where vortices with dipolar interactions are considered, the derivation of the vortex interactions in the London limit is discussed, and results that were not included in the paper are discussed.

### 3.1 Hierarchical structure formation

In paper 1, the effects of pairwise vortex interactions with several repulsive and/or attractive length scales are analyzed using Monte Carlo methods and molecular dynamics simulations. Such interactions are argued to be possible by fabrication of layered superconducting structures with each layer having a different penetration depth, and/or layers of insulating materials of varying thickness, see paper 1 and references therein.

It is demonstrated that a variety of structures like giant clusters, ring clusters, voids, stripes and clusters of clusters (so-called *superclusters*) are possible depending on the shape of the interaction potential and density. A molecular dynamics follow-up paper demonstrated that honeycomb and kagome lattices are also possible [107] and argued that it could provide control of a magnetic lattice for ultracold atomic experiments.

An illustrative example obtained with Monte Carlo of hierarchical structure formation due to multi-scale repulsion is shown in Fig. 3.1. The melting of a particular case of such a superclustering phase is considered in Fig. 3.2 where it is seen that the melting can occur in two steps, corresponding to melting of the subclusters followed by melting of the superclusters. In Fig. 3.1 there are three repulsive scales and thus there can be clusters of clusters, but by adding more repulsive scales it is possible to have more steps of clustering of clusters, as shown in Fig. 3.3 where a four-step potential yields clusters of clusters of clusters.

### 3.2 Stripe phases due to non-pairwise interaction

In paper 2, an effective point-particle vortex model with interactions of the forms calculated from Ginzburg-Landau theory [34, 40] is studied. In a complicated field-theoretical description of vortices, they do not necessarily interact with purely pairwise interaction. In such systems vortices can interact with short-range repulsive and long-range attractive pairwise interaction, but also with a repulsive three-body interaction. A variety of phases like stripes, ‘gossamer’ (web-like) patterns and glassy phases can arise in the point-particle model. See Fig. 3.4 for an illustrative example of the stripe phase.

### 3.3 Vortices with dipolar forces

In paper 3, Ginzburg-Landau theory calculations and point-particle Monte Carlo are combined to study two-component systems where vortices core-split (see Fig. 3.6) giving rise to effective dipolar-like interactions. The paper considers a two-component Ginzburg-Landau theory and an associated London theory with a *dissipationless drag* term (3.1b) which gives

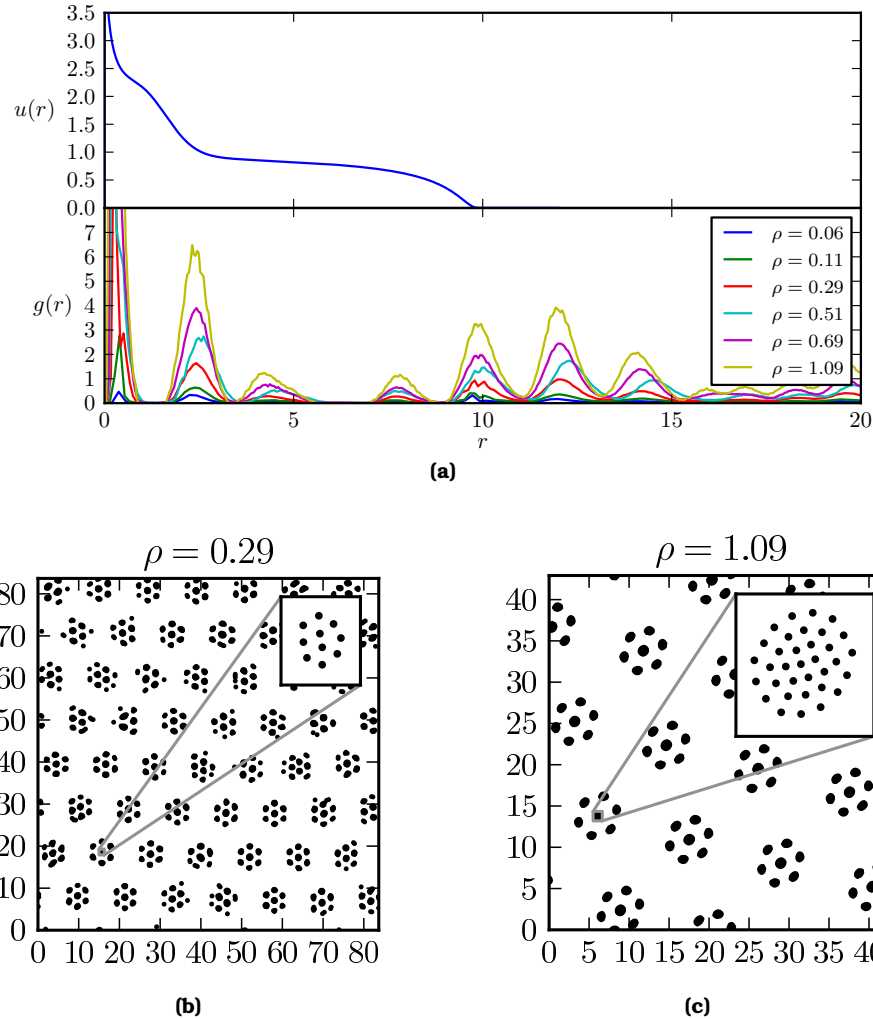


**Figure 3.1:** An illustrative example of hierarchical structure formation for 2000 particles. In a) we plot the interaction potential  $u(r) = [K_0(R) + e^{-(r-1)^2} + 1] \cdot e^{-1/(10-r)}$  (if  $r < 10$  and zero otherwise) and the radial distribution function  $g(r)$  for various densities  $\rho = N/L^2$ . In b) and c) the hierarchical patterns for two densities are plotted.

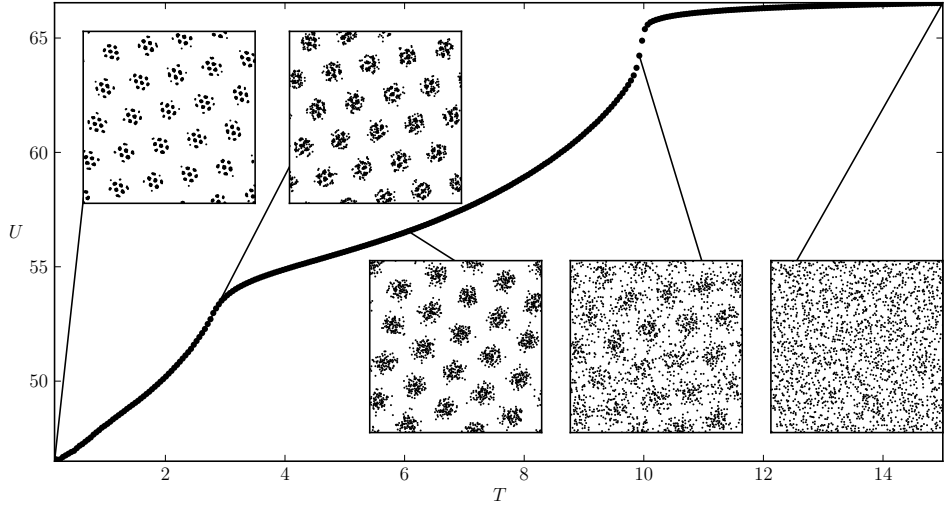


**Figure 3.2:** Melting of a superclustering phase for a three-step potential  $u(r)$  where  $u = \infty$  for  $r < 0.25$ ,  $u = 2.25$  for  $0.25 < r < 1.75$ ,  $u = 0.8$  for  $1.75 < r < 10$  and  $u = 0$  for  $r > 10$ , here with 2000 particles for a density  $\rho = N/L^2 = 0.51$ .  $U$  is the thermal average of the interaction energy and the insets show snapshots of the structure formation at the marked temperatures.

rise to skyrmions (to be discussed below, a dissipationless drag effect is furthermore the main focus of paper 5). For a multicomponent system, this drag term corresponds to current-current (Andreev-Bashkin) interactions of the form  $v_i \cdot v_j$  [111], and in the London limit we can consider the following free-energy density:

$$f = \frac{1}{2} \sum_{a=1,2} |\psi_a|^2 (\nabla \theta^{(a)} + e\mathbf{A})^2 \quad (3.1a)$$

$$+ \frac{1}{2} \nu \left| |\psi_1|^2 (\nabla \theta^{(1)} + e\mathbf{A}) + |\psi_2|^2 (\nabla \theta^{(2)} + e\mathbf{A}) \right|^2 \quad (3.1b)$$

$$+ \frac{1}{2} (\nabla \times \mathbf{A})^2, \quad (3.1c)$$

where (3.1b) corresponds to the Andreev-Bashkin intercomponent drag term with strength determined by  $\nu$ , and the other two terms are the usual kinetic and magnetic energy density terms.

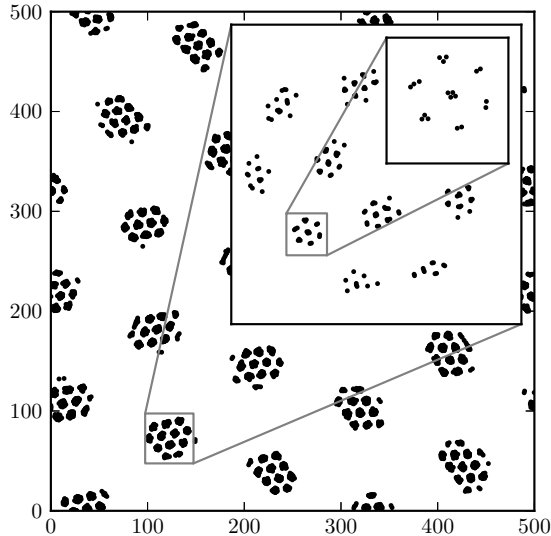


**Figure 3.3:** Clusters of clusters of clusters for an interaction with four repulsive scales. Here the potential  $u(r)$  is a four-step potential with  $u = \infty$  for  $r < 0.25$ ,  $u = 2.25$  for  $0.25 < r < 1.75$ ,  $u = 0.8$  for  $1.75 < r < 10$ ,  $u = 0.3$  for  $10 < r < 80$ , and  $u = 0$  for  $r > 80$ , and there are 5000 particles in a square box with a side length of 500.

### Skyrmions

A central result of paper 3 is that an Andreev-Bashkin interaction can stabilize *skyrmions* in two-component superconductors. A skyrmion is a topological object in which a three-dimensional unit texture  $\mathbf{n}$  assumes all possible values on the unit two-sphere<sup>1</sup>. Such objects can occur for instance in magnets, see Fig. 3.5 for a vortex skyrmion. While covering the plane, the number of wrappings around the unit sphere may be quantified by the topological skyrmion number

$$Q = \frac{1}{4\pi} \int dx dy \mathbf{n} \cdot \left( \frac{\partial \mathbf{n}}{\partial x} \times \frac{\partial \mathbf{n}}{\partial y} \right). \quad (3.2)$$

---

<sup>1</sup>For two-dimensional cases, as here, the objects are sometimes referred to as *baby* skyrmions [112].

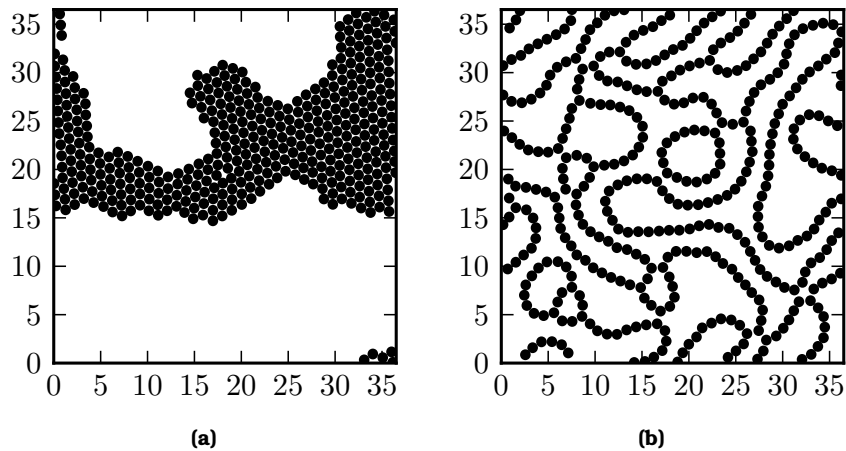


**Figure 3.4:** Structure formation obtained for a system with short-range repulsive and long-range attractive two-body interaction and a repulsive three-body interaction. In a) the three-body interaction is weak and the vortices form clusters. In b) the three-body interaction is strong and the vortices form stripes.

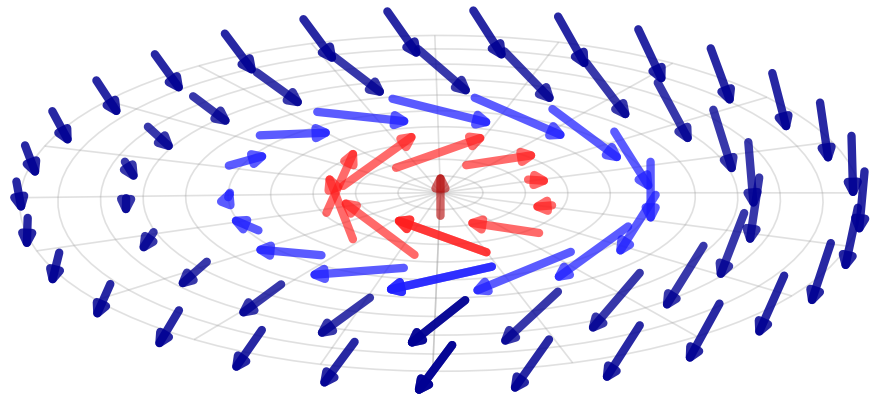


**Figure 3.5:** Illustration of a vortex skyrmion. Blue arrows point down, and red arrows point up.

To get a feeling of how the quantity (3.2) works, we follow the derivation in e.g. [113] and write

$$\mathbf{n} = \begin{pmatrix} \sin(\theta(r)) \cos(\Phi(\varphi)) \\ \sin(\theta(r)) \sin(\Phi(\varphi)) \\ \cos(\theta(r)) \end{pmatrix}, \quad (3.3)$$

where  $r$  and  $\varphi$  are the coordinates of a cylindrical system,  $\Phi$  and  $\theta$  are the polar and azimuthal angles of  $\mathbf{n}$ . Insertion into (3.2) yields after some computation

$$Q = \frac{1}{4\pi} \int_0^\infty dr \int_0^{2\pi} d\varphi \frac{d\theta(r)}{dr} \frac{d\Phi(\varphi)}{d\varphi} \sin(\theta(r)) \quad (3.4a)$$

$$= \frac{1}{4\pi} \left[ -\cos(\theta(r)) \right]_{r=0}^{r=\infty} \left[ \Phi(\varphi) \right]_{\varphi=0}^{\varphi=2\pi}. \quad (3.4b)$$

Since the skyrmion texture is such that  $\mathbf{n}$  switches pole from  $r = 0$  to  $r = \infty$ , for the case in Fig. 3.5 we then have  $[-\cos(\theta(r))]_{r=0}^{r=\infty} = 2$ , giving

$$Q = \frac{\left[ \Phi(\varphi) \right]_{\varphi=0}^{\varphi=2\pi}}{2\pi} \equiv m, \quad (3.5)$$

which we identify as the phase winding number  $m$  (vorticity).

Skyrmions may be identified in two-component superconductors when composite vortices (vortices with winding in both phases) core-split into fractional vortices. This can be understood through the mapping of the density-varying GL theory to an easy-plane non-linear sigma model  $\mathbf{n} = \Psi^\dagger \sigma \Psi / \Psi^\dagger \Psi$  where  $\Psi = (\psi_1, \psi_2)^T$  and  $\sigma = (\sigma_1, \sigma_2, \sigma_3)$  with  $\sigma_i$  the Pauli matrices. For details, we refer to paper 3. The texture of  $\mathbf{n}$  for a composite vortex core-splitting into fractional vortices is schematically shown in Fig. 3.6.

### Vortex interaction potentials

From (3.1) one can derive interaction potentials of vortices in the London limit. First, rewrite the free energy density (3.1) into the form:

$$f = \frac{1}{2} \frac{|\psi_1|^2 |\psi_2|^2}{|\psi_1|^2 + |\psi_2|^2} \left( \nabla(\theta^{(1)} - \theta^{(2)}) \right)^2 \quad (3.6a)$$

$$+ \frac{1}{2} \left( \frac{1}{|\psi_1|^2 + |\psi_2|^2} + \nu \right) \left( |\psi_1|^2 \nabla \theta^{(1)} + |\psi_2|^2 \nabla \theta^{(2)} + e(|\psi_1|^2 + |\psi_2|^2) \mathbf{A} \right)^2 \quad (3.6b)$$

$$+ \frac{1}{2} (\nabla \times \mathbf{A})^2. \quad (3.6c)$$

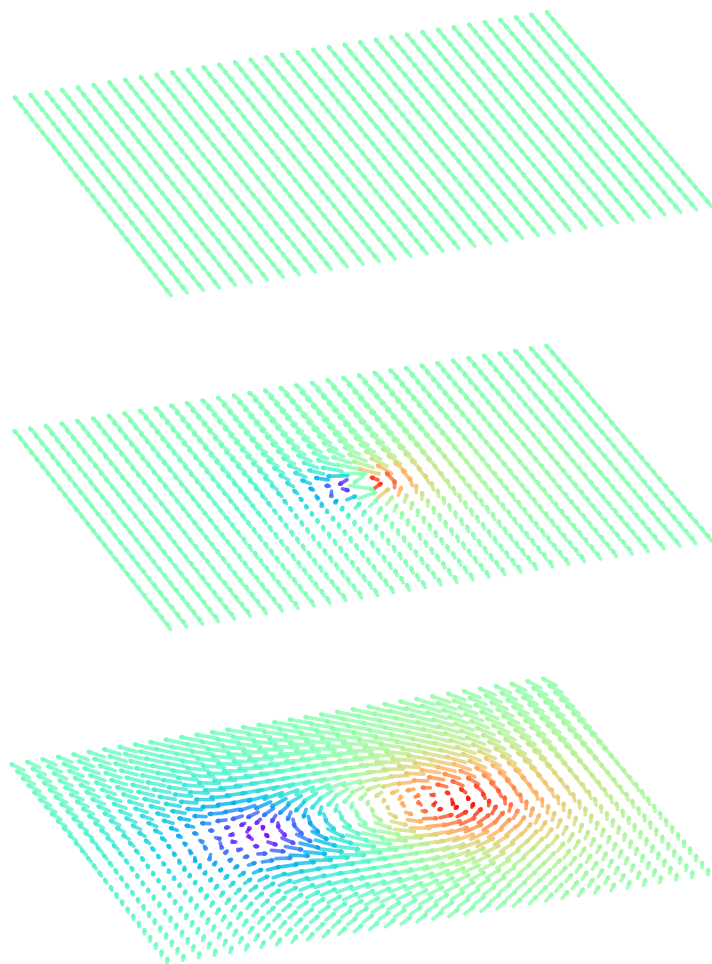


**Figure 3.6:** Schematic texture of  $n = \Psi^\dagger \sigma \Psi / \Psi^\dagger \Psi$  for a composite vortex core-splitting into fractional vortices, with core-splitting increasing from the upper to the lower plot, with no core-splitting in the upper-most plot. Red arrows point up, blue arrows point down, and green arrows point in-plane.

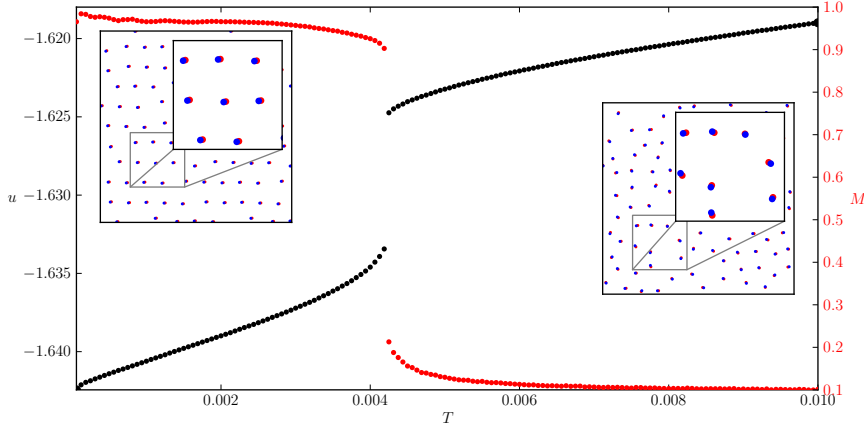


**Figure 3.7:** Melting of a dipolar lattice for  $|\psi_1|^2 + |\psi_2|^2 = 4.125$ ,  $m = 2.1429$ ,  $e = 0.8$ ,  $\nu = 0.025$ ,  $N = 198$  and density  $\rho = 0.04$ . Red and blue dots correspond to vortices from different components. On the left axis is the internal energy per particle and the quantity  $M$  on the right (red) axis is a measure of the alignment of the dipoles.

In this expression, (3.6a) is called the neutral mode since it does not contain any terms with  $e$ , and thus (3.6b) is the charged mode. We can derive the interaction potentials by considering contributions from the charged and neutral modes separately. Setting  $\nabla\theta^{(1)} = \nabla\theta^{(2)} = 0$  we get the free energy associated with excitations in  $\mathbf{A}$  which is

$$f = \frac{1}{2}(ke\mathbf{A})^2 + \frac{1}{2}(\nabla \times \mathbf{A})^2, \quad (3.7)$$

with  $k = \sqrt{(|\psi_1|^2 + |\psi_2|^2)(1 + \nu(|\psi_1|^2 + |\psi_2|^2))}$ . We now make the ansatz  $\mathbf{A} = -g(r)\hat{\phi}$  in cylindrical coordinates and look for non-trivial solutions. For the second term in (3.7) we then have

$$\nabla \times \mathbf{A} = -\frac{1}{r}\frac{\partial}{\partial r}\left(rg(r)\right)\hat{z}. \quad (3.8)$$

The total free energy is then (omitting a constant prefactor)

$$\int r dr \left( (ke)^2 g^2 + \frac{g^2}{r^2} + \frac{2gg'}{r} + (g')^2 \right) = \int dr L[r, g, g'], \quad (3.9)$$

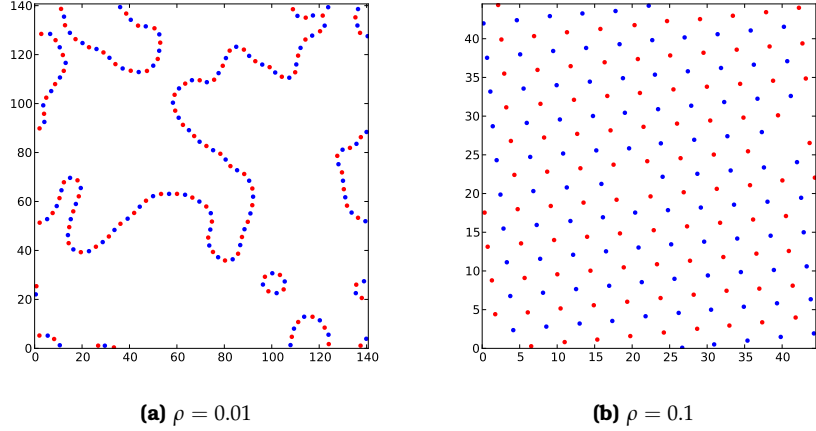


**Figure 3.8:** Two examples of possible structure formations for skyrmions with dipolar forces. Loops and checkerboard lattices can occur for low and high density  $\rho = N/L^2$  respectively, with  $|\psi_1|^2 + |\psi_2|^2 = 2$ ,  $m = 1$ ,  $e = 0.6$ ,  $\nu = 2$  and  $N = 198$ .

which presents a variational problem to find the  $g(r)$  that minimizes the total free-energy functional. Since

$$\frac{\partial L}{\partial g} = 2 \left( (ke)^2 r + \frac{1}{r} \right) g + 2g', \quad (3.10a)$$

$$\frac{\partial}{\partial r} \frac{\partial L}{\partial g'} = 2g' + 2(rg')', \quad (3.10b)$$

the Euler-Lagrange equation gives

$$\left( (ke)^2 r + r^{-1} \right) g - (rg')' = 0. \quad (3.11)$$

The physical solution is a first order modified Bessel function of the second kind ( $C$  is a constant)

$$g(r) = C \cdot K_1(ker), \quad (3.12)$$

from which we can identify the penetration depth  $\lambda = 1/ke$ ,

$$\lambda = \frac{1}{e \sqrt{(|\psi_1|^2 + |\psi_2|^2)(1 + \nu(|\psi_1|^2 + |\psi_2|^2))}}. \quad (3.13)$$

The constant  $C$  can be determined to be  $C = \phi_0/2\pi\lambda$  with  $\phi_0 = 2\pi/e$  the flux quantum, see e.g. [51]. The magnetic field then becomes

$$B(r) = \frac{\phi_0}{2\pi\lambda^2} K_0 \left( \frac{r}{\lambda} \right). \quad (3.14)$$

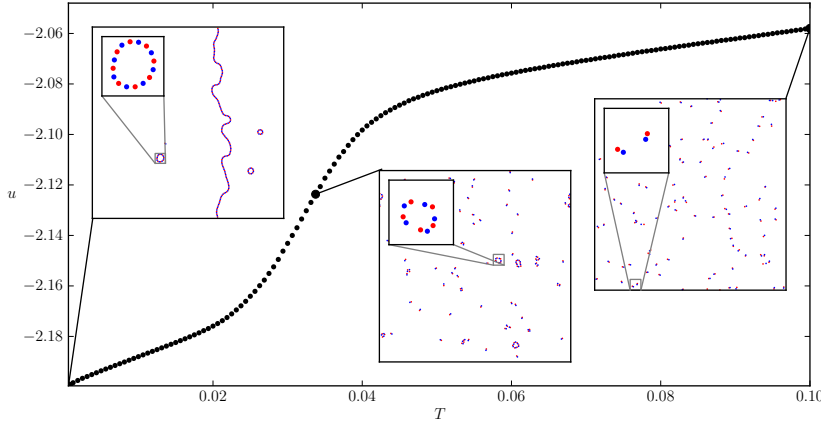


**Figure 3.9:** Melting of a loop phase with  $|\psi_1|^2 + |\psi_2|^2 = 4.125$ ,  $m = 2.1429$ ,  $e = 0.8$ ,  $\nu = 1.0$ ,  $N = 198$  and  $\rho = 0.001$ , for which at the highest temperature shown the vortices are still bound in pairs, and at even higher temperatures (not shown) such pairing is also broken.

The vortex interaction energy can now be calculated using  $A = -\lambda^2 \nabla \times B$ , the vector identities  $(\nabla \times B)^2 = B \cdot \nabla \times \nabla \times B + \nabla \cdot (B \times \nabla \times B)$  and  $\nabla \times \nabla \times B = \nabla(\nabla \cdot B) - \nabla^2 B$ , as well as  $-\nabla^2 K_0(r/\lambda) + K_0(r/\lambda)/\lambda^2 = 2\pi\delta(r)$  [51]. Consider a vortex belonging to component  $a$  (where  $a$  is either 1 or 2) positioned at  $\mathbf{r}_a$ , and a vortex belonging to component  $b$  ( $b$  is also either 1 or 2) at  $\mathbf{r}_b$  we get the energy contribution corresponding to (3.7)

$$E_{ab}^{\text{charged}} = \frac{1}{2} \int dS \left( \frac{\phi_a}{2\pi\lambda^2} K_0 \left( \frac{|\mathbf{r} - \mathbf{r}_a|}{\lambda} \right) + \frac{\phi_b}{2\pi\lambda^2} K_0 \left( \frac{|\mathbf{r} - \mathbf{r}_b|}{\lambda} \right) \right) \times \quad (3.15a)$$

$$\times (\phi_a \delta(\mathbf{r} - \mathbf{r}_a) + \phi_b \delta(\mathbf{r} - \mathbf{r}_b)) \quad (3.15b)$$

$$= \frac{\phi_a \phi_b}{2\pi\lambda^2} K_0 \left( \frac{|\mathbf{r}_a - \mathbf{r}_b|}{\lambda} \right) + \text{self-energy terms}. \quad (3.15c)$$

Each vortex carries a fraction of the flux quantum  $\phi_0$  which is given by  $\phi_a = \phi_0 |\psi_a|^2 / (|\psi_1|^2 + |\psi_2|^2)$  [7, 51]. Writing  $r = |\mathbf{r}_a - \mathbf{r}_b|$  the interactions due to the charged mode take the form

$$E_{12}^{\text{charged}} = 2\pi |\psi_1|^2 |\psi_2|^2 \left( \frac{1}{|\psi_1|^2 + |\psi_2|^2} + \nu \right) K_0 \left( \frac{r}{\lambda} \right), \quad (3.16a)$$

$$E_{aa}^{\text{charged}} = 2\pi |\psi_a|^4 \left( \frac{1}{|\psi_1|^2 + |\psi_2|^2} + \nu \right) K_0 \left( \frac{r}{\lambda} \right). \quad (3.16b)$$

Next, consider the contributions from the neutral mode (3.6a). Assuming that  $\theta^{(a)} = \theta$  where  $\theta$  is the polar angle, gives

$$\nabla\theta^{(a)} = \nabla\theta = \frac{1}{\rho}\hat{\theta} = \hat{\mathbf{z}} \times \nabla \ln(|\mathbf{r} - \mathbf{r}_a|). \quad (3.17)$$

The interaction energy due to the neutral mode for two vortices  $a \neq b$  is calculated with the divergence theorem<sup>2</sup> and using  $\nabla^2 \ln r = 2\pi\delta(\mathbf{r})$  as follows

$$E_{a \neq b}^{\text{neutral}} = \frac{1}{2} \frac{|\psi_1|^2 |\psi_2|^2}{|\psi_1|^2 + |\psi_2|^2} \int dS (\nabla(\theta^{(1)} - \theta^{(2)}))^2 \quad (3.18a)$$

$$= -\frac{|\psi_1|^2 |\psi_2|^2}{|\psi_1|^2 + |\psi_2|^2} \int dS \nabla\theta^{(1)} \cdot \nabla\theta^{(2)} + \text{self-energy terms} \quad (3.18b)$$

$$= \frac{|\psi_1|^2 |\psi_2|^2}{|\psi_1|^2 + |\psi_2|^2} \int dS \theta^{(1)} \nabla^2 \theta^{(2)} \quad (3.18c)$$

$$= \frac{|\psi_1|^2 |\psi_2|^2}{|\psi_1|^2 + |\psi_2|^2} \int dS \ln(|\mathbf{r} - \mathbf{r}_1|) \cdot 2\pi\delta(\mathbf{r} - \mathbf{r}_2) \quad (3.18d)$$

$$= 2\pi \frac{|\psi_1|^2 |\psi_2|^2}{|\psi_1|^2 + |\psi_2|^2} \ln(|\mathbf{r}_1 - \mathbf{r}_2|). \quad (3.18e)$$

For two vortices 1 and 2, in the same component  $a$ , we have  $\theta^{(a)} = \theta_1^{(a)} + \theta_2^{(a)}$  while  $\theta^{(b)} = 0$  and the calculation is identical to the one in (3.18) but with the sign reversed. The interaction energies due to the neutral mode are thus

$$E_{12}^{\text{neutral}} = 2\pi \frac{|\psi_1|^2 |\psi_2|^2}{|\psi_1|^2 + |\psi_2|^2} \ln(r), \quad (3.19a)$$

$$E_{aa}^{\text{neutral}} = -2\pi \frac{|\psi_1|^2 |\psi_2|^2}{|\psi_1|^2 + |\psi_2|^2} \ln(r). \quad (3.19b)$$

with  $r = |\mathbf{r}_1 - \mathbf{r}_2|$ . Putting together (3.16) and (3.19) gives

$$E_{12} = \ln\left(\frac{r}{R}\right) + wK_0\left(\frac{r}{\lambda}\right), \quad (3.20a)$$

$$E_{11} = -\ln\left(\frac{r}{R}\right) + mwK_0\left(\frac{r}{\lambda}\right), \quad (3.20b)$$

$$E_{22} = -\ln\left(\frac{r}{R}\right) + \frac{w}{m}K_0\left(\frac{r}{\lambda}\right), \quad (3.20c)$$

where  $w = 1 + v(|\psi_1|^2 + |\psi_2|^2)$  and  $m = |\psi_1|^2 / |\psi_2|^2$ .

---

<sup>2</sup> $\int_S dS \nabla \cdot \mathbf{F} = \oint_C \hat{\mathbf{n}} ds \cdot \mathbf{F} = 0$  with  $\mathbf{F} = \theta^{(1)} \nabla \theta^{(2)}$ .

### Results from Monte Carlo simulations

The potentials (3.20) allow for a variety of structures like checkerboard lattices, octagonal structures and rings, which can also arise in the Ginzburg-Landau setting. For small core-splitting, the vortices can form a dipolar lattice as shown in Fig. 3.7. When the core-splitting is large, loops and strings can occur at low densities, and square lattices for high densities, see Figs. 3.8 and 3.9.

We also comment on the Monte Carlo updates that one can use for systems with several kinds of particles. Making only single-particle displacement trial moves might be inefficient if particles are bound. For the case here, were the particles form bound pairs, an obvious multi-body displacement trial move is to chose a particle, determine its corresponding paired particle, and make a pairwise displacement or a pairwise rotation around their center of mass. For situations where the particles are tightly paired, displacement moves where particles switches paired neighbors would be rare and the simulation essentially balanced. However, if such a multi-body trial move causes particles to switch their paired partners, the next trial move will be unbalanced. To circumvent this, it is possible to either keep a fixed list of paired particles, and to update this list infrequently enough. For example, it is common to adjust the step size of trial moves to fix the acceptance ratio, which can reduce correlations. However, such adjustment also introduces errors as they cause the breaking of balance as well as the breaking of the Markovian property of the simulation [114]. However, it has been shown [115] that if step length adjustments are made infrequently enough, the introduced error can be smaller than the statistical error. It can thus actually improve a Monte Carlo simulation to break balance, if proper care is taken. Another strategy is to make balance-breaking trial moves only during a first part of the equilibration, so that the simulation could faster reach low-energy configurations, and thereafter only using balance-preserving moves during a remaining warm up and subsequent data gathering.



## **Chapter 4**

# **Phase transitions in multicomponent London superconductors**

In one-component three-dimensional  $U(1)$  lattice London superconductors, the phase transition is known to be in the “inverted-3DXY” universality class, as was shown by a duality mapping [13] and subsequent Monte Carlo simulations [14]. In the two-component case, the phase transition can by contrast be first-order, as was shown for  $U(1) \times U(1)$  systems [15, 16, 17, 18], in the absence of a so-called *Josephson coupling*. The Josephson coupling is an intercomponent interaction which corresponds to intercomponent tunneling of Cooper pairs [116, 51], giving a coupling  $|\psi_a||\psi_b| \cos(\theta^{(a)} - \theta^{(b)})$  between components  $a$  and  $b$ . Such terms then break the symmetry down to  $U(1)$ , which leads to the question of what happens to the first-order phase transition when such an interaction is taken into account. This question is the study of paper 4, with the main result that the phase transition can be first-order for small Josephson couplings and continuous for large Josephson couplings. The finite-size scaling arguments for this conclusion is contained in the paper, the following sections contain details of the derivation of length scales and discretization of the model and is concluded with results from Monte Carlo calculations that were not included in paper 4.

### **4.1 Two-component London superconductivity**

We now consider an extension of the one-component Ginzburg-Landau free energy (1.1) to a two-component theory with components  $a = 1, 2$ , and take the limit of constant amplitudes  $|\psi_a|$  (the London limit). We then have  $\psi_a(\mathbf{r}) = |\psi_a| e^{i\theta^{(a)}(\mathbf{r})}$  with  $|\psi_a|^2 = \text{a positive constant}$ . The gradient terms of

the Ginzburg-Landau free energy then becomes  $\nabla\psi_a = \psi_a i\nabla\theta^{(a)}$  so that  $|(\nabla + ie\mathbf{A})\psi_a|^2 = |\psi_a i\nabla\theta^{(a)} + ie\mathbf{A}\psi_a|^2 = |\psi_a|^2(\nabla\theta^{(a)} + e\mathbf{A})^2$ . Since the constant  $|\psi_a|^2$  determines the energetic cost associated with phase gradients, it is sometimes called a *phase stiffness*. By including a Josephson interaction term we then have free-energy density

$$f = \sum_{a=1,2} \frac{1}{2} |\psi_a|^2 (\nabla\theta^{(a)} + \mathbf{A})^2 \quad (4.1a)$$

$$+ \frac{1}{2e^2} (\nabla \times \mathbf{A})^2 \quad (4.1b)$$

$$+ \eta |\psi_1| |\psi_2| \cos(\theta^{(1)} - \theta^{(2)}), \quad (4.1c)$$

where the last term is the Josephson interaction with strength given by the parameter  $\eta$ .

In (4.1) two characteristic length scales can be identified, namely the Josephson length  $\xi_J$ , and the magnetic penetration depth  $\lambda$ . We shall below derive formulas for these scales in terms of the defining parameters of the model (the ground-state amplitudes  $|\psi_1|$  and  $|\psi_2|$ , the charge coupling  $e$  and the Josephson coupling  $\eta$ ), and rewrite our model in terms of the two length scales:

$$f = \frac{1}{2} \sum_{a=1,2} |\psi_a|^2 (\nabla\theta^{(a)} + \mathbf{A})^2 \quad (4.2a)$$

$$+ \frac{1}{2} \lambda^2 (|\psi_1|^2 + |\psi_2|^2) (\nabla \times \mathbf{A})^2 \quad (4.2b)$$

$$+ \frac{1}{\xi_J^2} \frac{|\psi_1|^2 |\psi_2|^2}{|\psi_1|^2 + |\psi_2|^2} \cos(\theta^{(1)} - \theta^{(2)}), \quad (4.2c)$$

where  $\lambda$  is the penetration depth and  $\xi_J$  the Josephson length. The penetration depth  $\lambda$  is obtained by setting  $v = 0$  in (3.13) giving

$$\lambda = \frac{1}{e \sqrt{|\psi_1|^2 + |\psi_2|^2}}. \quad (4.3)$$

The Josephson length  $\xi_J$  is derived below.

## 4.2 Derivation of the Josephson length $\xi_J$

We follow [117] and imagine that we are in the ground state where there are no phase gradients and the phases are locked. Assume that  $\eta$  is positive, consider one dimension  $x$  and write<sup>1</sup>

$$\theta^{(1)} - \theta^{(2)} = \pi + \delta(x), \quad (4.4)$$

---

<sup>1</sup>Note that  $\delta(x)$  here is not the Dirac delta function.

where the total free energy due to the phase difference is minimized when  $\delta(x) = 0$  everywhere. We have  $\nabla(\theta^{(1)} - \theta^{(2)}) = \delta'(x)$  and  $\cos(\theta^{(1)} - \theta^{(2)}) = \cos(\pi + \delta(x)) = -\cos(\delta(x))$ . Imagine that the phase difference is perturbed slightly from its ground state value at  $x = 0$ . By enforcing that  $\delta(0) = \delta_0$ , the response of the system can be found by calculating the profile  $\delta(x)$  which minimizes the total free energy. The gradient term opposes any spatial changes in the phase difference and the phase locking term favors that  $\delta(x)$  goes to zero. The  $\delta(x)$  which optimizes these competing tendencies is found by minimizing the functional

$$\int dx \left[ \frac{1}{2} \frac{|\psi_1|^2 |\psi_2|^2}{|\psi_1|^2 + |\psi_2|^2} (\delta'(x))^2 - \eta |\psi_1| |\psi_2| \cos(\delta(x)) \right] = \int dx L[x, \delta, \delta']. \quad (4.5)$$

We have that  $\partial L / \partial \delta = \eta |\psi_1| |\psi_2| \sin(\delta)$  and  $(d/dx)(\partial L / \partial \delta') = \delta'' |\psi_1|^2 |\psi_2|^2 / (|\psi_1|^2 + |\psi_2|^2)$  which after expanding  $\sin(\delta(x))$  and omitting higher order terms gives from the Euler-Lagrange equation

$$\delta''(x) - \frac{\eta(|\psi_1|^2 + |\psi_2|^2)}{|\psi_1| |\psi_2|} \delta(x) = 0, \quad (4.6)$$

with the physical solution

$$\delta(x) = \delta_0 \exp \left( -\frac{x}{\xi_J} \right), \quad (4.7)$$

where the characteristic length scale associated with the return of the system to the ground state is the Josephson length

$$\xi_J = \sqrt{\frac{|\psi_1| |\psi_2|}{\eta(|\psi_1|^2 + |\psi_2|^2)}}. \quad (4.8)$$

### 4.3 Discretization of the two-component London free energy

We begin by describing the notation used in the discretization. We define a square lattice in three dimensions with isotropic lattice spacing  $h$ . All vectors are Cartesian vectors with  $\mathbf{C} = (C_x, C_y, C_z) = C_x \hat{\mathbf{x}} + C_y \hat{\mathbf{y}} + C_z \hat{\mathbf{z}}$ . A site is indexed by  $i$  so that  $H = \sum_i (H)_i$  where  $\sum_i$  means “sum over all sites  $i$ ” and  $(H)_i$  denotes the discretized value of  $H$  at site  $i$ , the discretized value of the vector  $\mathbf{C}$  on site  $i$  is denoted  $(\mathbf{C})_i$ , the  $\mu$ -component of a vector  $\mathbf{C}$  is denoted by  $[\mathbf{C}]_\mu = C_\mu$ , the  $\mu$ -component of the vector  $(\mathbf{C})_i$  is denoted  $([\mathbf{C}]_\mu)_i = C_{i\mu}$  so that we can write  $(\mathbf{C})_i = (C_{ix}, C_{iy}, C_{iz})$  and the value of a scalar  $\mathbf{C}^2$  on the lattice site  $i$  is likewise denoted  $(\mathbf{C}^2)_i$ . Since a vector squared is the sum of its squared components we can then write  $\mathbf{C}^2 =$

$\mathbf{C} \cdot \mathbf{C} = C_x C_x + C_y C_y + C_z C_z = C_x^2 + C_y^2 + C_z^2 = \sum_{\mu=x,y,z} C_\mu^2 = \sum_{\mu=x,y,z} [\mathbf{C}]_\mu^2$ , and for brevity denote  $\sum_{\mu=x,y,z}$  by  $\sum_\mu$ . Thus we can write the value of the square of the vector  $\mathbf{C}$  at site  $i$  as

$$(\mathbf{C}^2)_i = \left( \sum_\mu [\mathbf{C}]_\mu^2 \right)_i = \sum_\mu ([\mathbf{C}]_\mu^2)_i = \sum_\mu C_{i\mu}^2. \quad (4.9)$$

On every site we have five variables: the two phases  $\theta_i^{(1)}, \theta_i^{(2)}$  and the three components of the vector  $(\mathbf{A})_i$ :  $A_{ix}, A_{iy}$  and  $A_{iz}$ .

The Josephson term is trivially discretized by

$$\left( \frac{1}{\xi_J^2} \cos(\theta^{(1)} - \theta^{(2)}) \right)_i = \frac{1}{\xi_J^2} \cos(\theta_i^{(1)} - \theta_i^{(2)}) \quad (4.10a)$$

$$= \frac{1}{h^2} \left( \frac{h}{\xi_J} \right)^2 \cos(\theta_i^{(1)} - \theta_i^{(2)}), \quad (4.10b)$$

where the last step is performed for reason that will become apparent.

The gradient term of the kinetic energy density is discretized straightforwardly by the finite difference approximation

$$([\nabla \theta^{(a)}]_\mu)_i = \frac{\theta_{i+\hat{\mu}}^{(a)} - \theta_i^{(a)}}{h}. \quad (4.11)$$

We now rewrite the terms in our Hamiltonian to get the discretized kinetic energy of component  $a$  on site  $i$  as

$$\left( (\nabla \theta^{(a)} + \mathbf{A})^2 \right)_i = \left( \sum_\mu [\nabla \theta^{(a)} + \mathbf{A}]_\mu^2 \right)_i \quad (4.12a)$$

$$= \frac{1}{h^2} \sum_\mu (\theta_{i+\hat{\mu}}^{(a)} - \theta_i^{(a)} + h A_{i\mu})^2. \quad (4.12b)$$

To discretize the magnetic field energy density term we use the definition of the curl of a vector field  $\nabla \times \mathbf{C}$  at some point  $\mathbf{r}$  as the limit

$$(\nabla \times \mathbf{C}) \cdot \hat{\mathbf{n}} = \lim_{S \rightarrow 0} \frac{1}{|S|} \oint_{\partial S} \mathbf{C} \cdot d\mathbf{r}, \quad (4.13)$$

where  $S$  is some small surface around  $\mathbf{r}$  with a unit normal  $\hat{\mathbf{n}}$ , and  $\partial S$  is the boundary of  $S$ ,  $|S|$  is the area of  $S$ , with the direction of the curve  $\partial S$  defined by the right-hand rule. On our square lattice  $\partial S$  is a square with area  $h^2$  and with boundary that we denote by  $\square$ , which gives  $(\nabla \times \mathbf{C}) \cdot \hat{\mathbf{n}} \approx h^{-2} \oint_{\square} \mathbf{C} \cdot d\mathbf{r}$ . The unit normal is either  $\hat{\mathbf{n}} = \hat{x}$ ,  $\hat{\mathbf{n}} = \hat{y}$  or  $\hat{\mathbf{n}} = \hat{z}$ . We introduce the notation

$x' = y$ ,  $y' = z$ ,  $z' = x$ , and  $x'' = y' = z$ , etc., so that we can write the discrete lattice curl on site  $i$  in the plane with normal  $\hat{\mu}$  as (see Fig. 4.1)

$$(\nabla \times \mathbf{C} \cdot \hat{\mu})_i = \left( \frac{1}{h^2} \oint_{\square} \mathbf{C} \cdot d\mathbf{r} \right)_i \quad (4.14a)$$

$$= \frac{1}{h^2} \int_i^{i+\hat{\mu}'} \mathbf{C} \cdot \hat{\mu}' d\mu' + \frac{1}{h^2} \int_{i+\hat{\mu}'}^{i+\hat{\mu}'+\hat{\mu}''} \mathbf{C} \cdot \hat{\mu}'' d\mu'' \quad (4.14b)$$

$$+ \frac{1}{h^2} \int_{i+\hat{\mu}'+\hat{\mu}''}^{i+\hat{\mu}''} \mathbf{C} \cdot \hat{\mu}' d\mu' + \frac{1}{h^2} \int_{i+\hat{\mu}''}^i \mathbf{C} \cdot \hat{\mu}'' d\mu'' \quad (4.14c)$$

$$= \frac{1}{h^2} (hC_{i\mu'} + hC_{i+\hat{\mu}',\mu''} - hC_{i+\hat{\mu}'',\mu'} - hC_{i\mu''}). \quad (4.14d)$$

In the last line we can identify the discrete lattice curl with a unit grid spacing which we denote

$$[\Delta \times \mathbf{C}]_{i\mu} \equiv C_{i\mu'} + C_{i+\hat{\mu}',\mu''} - C_{i+\hat{\mu}'',\mu'} - C_{i\mu''}. \quad (4.15)$$

We then have that  $(\nabla \times \mathbf{A} \cdot \hat{\mu})_i = [\Delta \times h\mathbf{A}]_{i\mu}/h^2$  and can write the magnetic field energy density as

$$\left( \lambda^2 (\nabla \times \mathbf{A})^2 \right)_i = \lambda^2 \left( \sum_{\mu} [\nabla \times \mathbf{A}]_{i\mu}^2 \right)_i \quad (4.16a)$$

$$= \lambda^2 \sum_{\mu} \left( (\nabla \times \mathbf{A} \cdot \hat{\mu})_i \right)^2 \quad (4.16b)$$

$$= \lambda^2 \sum_{\mu} \left( \frac{1}{h^2} [\Delta \times h\mathbf{A}]_{i\mu} \right)^2 \quad (4.16c)$$

$$= \frac{1}{h^2} \left( \frac{\lambda}{h} \right)^2 \sum_{\mu} [\Delta \times h\mathbf{A}]_{i\mu}^2. \quad (4.16d)$$

## 4.4 Two-component lattice London superconductivity

Absorb the grid spacing into the length scales by the following redefinitions

$$h\mathbf{A} \rightarrow \mathbf{A}, \quad (4.17a)$$

$$\lambda/h \rightarrow \lambda, \quad (4.17b)$$

$$\xi_J/h \rightarrow \xi_J, \quad (4.17c)$$

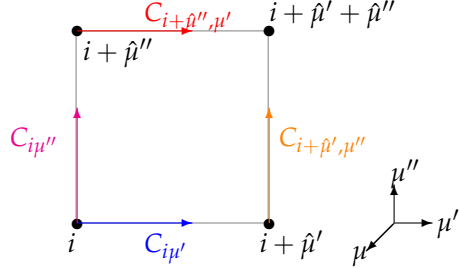


**Figure 4.1:** Lattice curl with  $\hat{\mu}$  normal to the plane square surface.

the Hamiltonian at  $i$  can then be expressed as

$$h^2(H)_i = \sum_{\mu} \sum_a |\psi_a|^2 (\theta_{i+\hat{\mu}}^{(a)} - \theta_i^{(a)} + A_{i\mu})^2 / 2 \quad (4.18a)$$

$$+ \lambda^2 (|\psi_1|^2 + |\psi_2|^2) \sum_{\mu} [\Delta \times \mathbf{A}]_{i\mu}^2 / 2 \quad (4.18b)$$

$$+ \frac{1}{\xi_J^2} \frac{|\psi_1|^2 |\psi_2|^2}{|\psi_1|^2 + |\psi_2|^2} \cos(\theta_i^{(1)} - \theta_i^{(2)}). \quad (4.18c)$$

We can absorb the grid spacing into the Hamiltonian by redefining  $h^2(H)_i \rightarrow (H)_i$ , and after rewriting the kinetic energy term into XY-model terms ( $\cos x \approx 1 - x^2/2$  so that  $x^2 \approx -2 \cos x + 2$ ) we obtain the final discretized Hamiltonian

$$H = \sum_i \left[ \sum_{\mu} \sum_a -|\psi_a|^2 \cos(\theta_{i+\hat{\mu}}^{(a)} - \theta_i^{(a)} + A_{i\mu}) \right] \quad (4.19a)$$

$$+ \frac{1}{2} \lambda^2 (|\psi_1|^2 + |\psi_2|^2) \sum_{\mu} [\Delta \times \mathbf{A}]_{i\mu}^2 + \quad (4.19b)$$

$$+ \frac{1}{\xi_J^2} \frac{|\psi_1|^2 |\psi_2|^2}{|\psi_1|^2 + |\psi_2|^2} \cos(\theta_i^{(1)} - \theta_i^{(2)}). \quad (4.19c)$$

Paper 4 contains a finite-size scaling analysis for the case with twin components  $|\psi_a|^2 = |\psi_b|^2 = 1$  which concludes that the phase transition can be first-order for small Josephson couplings, and continuous for large Josephson couplings. The reason for the first-order phase transition is argued to be because of a fluctuation-induced attraction between vortex lines, leading to phase separation at the transition.

The vortex attraction for a two-dimensional cross-section of vortex lines may be seen from the vortex interaction potentials (3.20) by letting  $w =$

$m = 1$  (corresponding to having equal phase stiffnesses  $|\psi_a|^2 = |\psi_b|^2$  and no drag interaction) and considering the total energy of a pair of composite vortices. Without core-splitting, the composite vortices repel, but the energetic cost of core-splitting is small, and is thus not unlikely to happen at a finite temperature. One may thus find a situation where two composite vortices form two dipoles which are mutually attractive. This point-particle analysis does not account for a presence of a finite Josephson coupling. A finite Josephson coupling opposes the core-splitting, as may be illustrated by the results in Fig. 4.2, which shows snapshots from simulations of the three-dimensional lattice theory (4.19) of vortex phases where an external magnetic field has been applied<sup>2</sup> along the vertical axis of the system. The displayed quantity is the interpolated isosurface of the kinetic energy density. A sufficiently strong Josephson coupling would thus remove the fluctuation-induced attraction, making the transition continuous.

We include here also results for a finite-size system when varying the difference in the phase stiffnesses  $|\psi_a|^2$  as well as varying the Josephson interaction  $\eta$ . In Fig. 4.3, one of the phase stiffnesses is kept constant and the other is varied until they are equal. For a big difference, two peaks are visible in the heat capacity  $C$ , which then merges into one pronounced peak when the difference is small. In Fig. 4.4, the phase stiffness difference is kept constant and the Josephson coupling is increased, causing the two visible peaks to merge into one peak which is about the same height as the previous peaks.

---

<sup>2</sup>An external magnetic field is applied along the  $z$ -axis by decomposing the gauge field into a fluctuating part and an applied part [118],  $A = A_{\text{fluct}} + A_{\text{app}}$ , where  $A_{\text{app}} = 2\pi f y \hat{x}$  so that the corresponding magnetic induction  $B_{\text{app}} = \nabla \times A_{\text{app}} = -2\pi f \hat{z}$ , where the parameter  $f$  determines the ground-state vortex density in the  $xy$ -plane. Note that because of periodic boundary conditions, special care must be taken when choosing  $f$  and the size of the lattice in the  $y$ -direction.

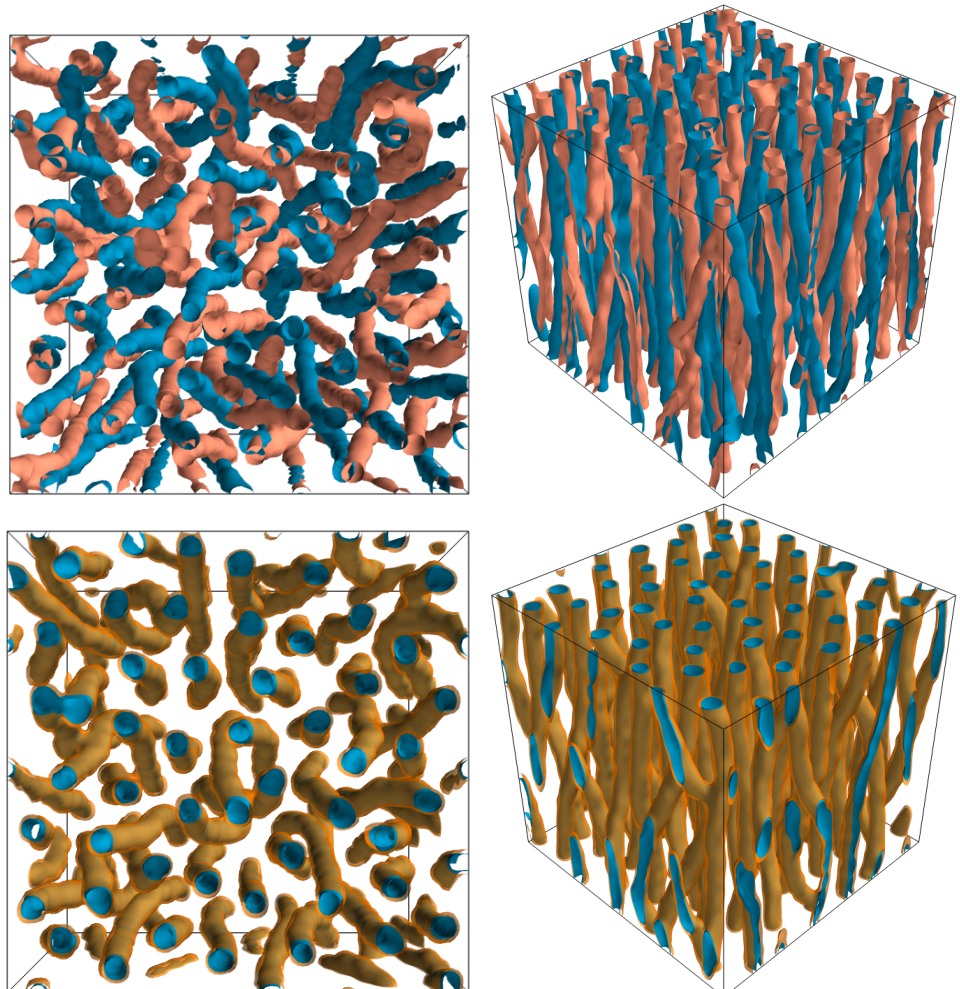


**Figure 4.2:** Top and perspective views of low-temperature vortex phases obtained for a two-component system with an applied magnetic field, where interpolated isosurface of the kinetic energy density are shown. The upper row is with a weak Josephson interaction, and the lower row is with a strong Josephson interaction, showing that the Josephson interaction opposes core-splitting of vortices.

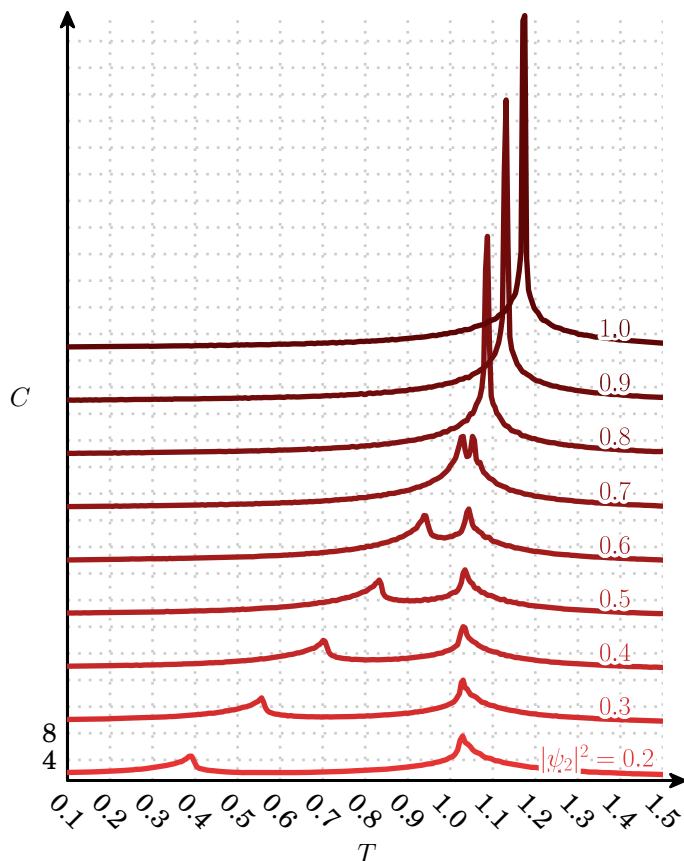


**Figure 4.3:** Heat capacities  $C$  versus temperature  $T$  for several systems of two-component lattice London superconductors where  $|\psi_1|^2 = 1.0$ ,  $e = 2.2$ ,  $\eta = 0$  and  $|\psi_2|^2$  varies. For a big difference between the phase stiffnesses  $|\psi_1|^2$  and  $|\psi_2|^2$  there can be two visible peaks in the heat capacity. For clarity, each curve is displaced vertically from the underlying curve in the figure. When the difference is decreased by increasing  $|\psi_2|^2$ , the peaks appear to merge into one more pronounced peak.

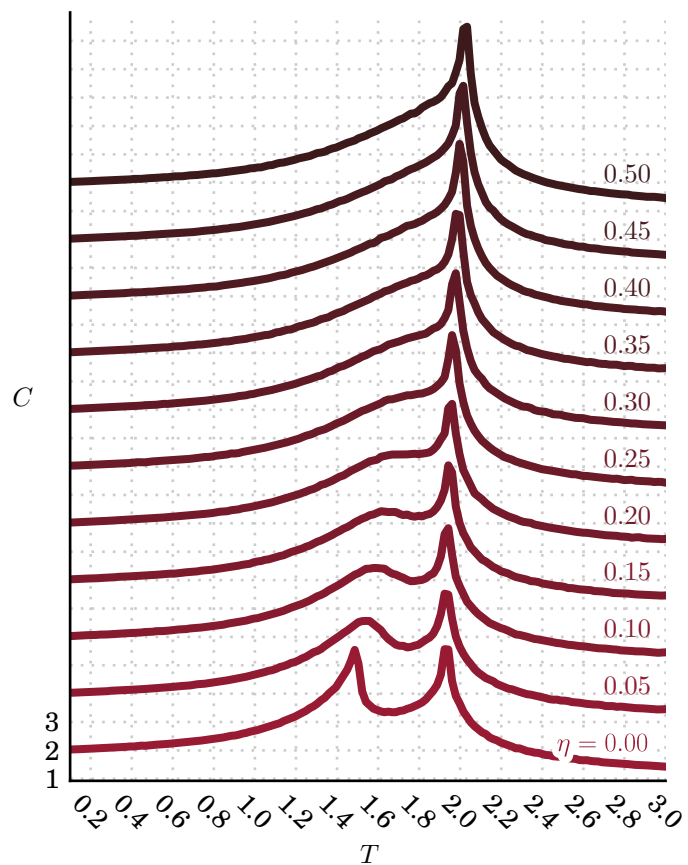


**Figure 4.4:** As in Fig. 4.3 but with  $|\psi_1|^2 = 0.8$ ,  $|\psi_2|^2 = 1.2$ ,  $e = 1$ ,  $L = 32$  and varying the Josephson coupling  $\eta$ . It is seen that the Josephson coupling  $\eta$  can cause a re-merging of peaks in the heat capacity.

## Chapter 5

# Drag interaction in the two-species Bose-Hubbard model

Paper 5 contains “worm” quantum Monte Carlo simulations of two-species ultracold bosons in optical lattices, with measurements of so-called *drag* interactions. The purpose of this chapter is to outline principles and details of such calculations. In chapter 1.4 superfluidity of helium was discussed, however the study of superfluidity is not restricted to helium. In the 1990s, Bose-Einstein condensation was first realized experimentally [119, 120] by cooling dilute gases of bosonic atoms to very low temperatures. Shortly thereafter there was a proposal to trap such systems in optical lattices [121] to essentially create an experimental setup that simulates the theoretical so-called Bose-Hubbard model which describes bosons living on a lattice and contains a superfluid phase. This was later experimentally realized [122]. This provides physicists an opportunity to study a quantum many body system using both experimental quantum simulations and theoretical calculations, see e.g. [123].

In two-component ultracold atomic systems the respective superfluid velocities interact via an Andreev-Bashkin drag interaction [111]. For a system with components  $a$  and  $b$  the effective free energy density is given by [51]

$$f = \frac{1}{2}(\rho_a - \rho_{ab})\mathbf{v}_a^2 + \frac{1}{2}(\rho_b - \rho_{ab})\mathbf{v}_b^2 + \rho_{ab}\mathbf{v}_a \cdot \mathbf{v}_b, \quad (5.1)$$

where  $\rho_a$  and  $\rho_b$  are superfluid densities and  $\mathbf{v}_a$  and  $\mathbf{v}_b$  are the superfluid velocities, and finally  $\rho_{ab}$  corresponds to the Andreev-Bashkin drag interaction. The superfluid densities can be calculated from quantum Monte Carlo simulations with the Pollock-Ceperley formula [77], for details, refer to paper 5. Thus we can calculate the Andreev-Bashkin interaction from quantum Monte Carlo simulations of models of ultracold atoms in optical lattices. For this, we need to first go through the Bose-Hubbard model,

and how it can be efficiently simulated using the *worm* quantum Monte Carlo algorithm [78, 79]. We will discuss the one-component case below and omit details of the extension to the two-component case.

### 5.1 The Bose-Hubbard model

The Bose-Hubbard (BH) model with onsite interaction is given here by

$$H = -t \sum_{\langle ij \rangle} a_i^\dagger a_j + \frac{U}{2} \sum_i n_i(n_i - 1) - \mu \sum_i n_i, \quad (5.2)$$

which can be seen as a finite difference approximation to a second quantized Hamiltonian, see e.g. [124]. In Fig. 5.1 the model is illustrated. The first term with the hopping parameter  $t$  corresponds to jumps between neighboring lattice sites ( $a_i$ ,  $a_i^\dagger$  are the annihilation and creation operators respectively for site  $i$ ), the second term given by the potential  $U$  corresponds to an on-site pairwise interaction ( $U_{ij} = U\delta_{ij}$ ) and the last term with  $\mu$  corresponds to a chemical potential (which we restrict as spatially independent). Note that the two terms in (5.2) that are linear in  $n$  can be collected by absorbing a  $-U/2$ -term into the chemical potential with the redefinition  $\mu \rightarrow \mu - U/2$ , which we will use in the treatment to come.

The phase diagram of the BH model can be studied using various techniques, for a mean-field treatment see e.g. [125, 126]. Early quantum Monte Carlo simulations for a one-dimensional case with and without disorder were performed in [127]. A mean-field phase diagram for a one-dimensional BH model is shown in Fig. 5.2, where the characteristic lobe structure that separate Mott insulating (MI) and superfluid (SF) regions is seen. The first MI-SF lobes of the two-dimensional [128] and three-dimensional [129] cases have been determined with quantum Monte Carlo simulations which shows a qualitatively similar structure.

In the small  $U$  limit the ground-state energy for a one-dimensional case with unity filling factor can be obtained by Bogoliubov transformation [130]

$$\frac{E_0}{L} = -3t + \frac{\sqrt{2Ut}}{\pi} + \frac{U+2t}{\pi} \arccos \left( \sqrt{\frac{U}{U+2t}} \right). \quad (5.3)$$

In the small  $t$  limit the ground-state energy up to order 14 in  $x = t/U$  can be given by the expansion [131]

$$\frac{E_0}{4UL} = -x^2 + x^4 + \frac{68}{9}x^6 - \frac{1267}{81}x^8 + \frac{44171}{1458}x^{10} - \frac{4902596}{6561}x^{12} - \frac{8020902135607}{2645395200}x^{14}. \quad (5.4)$$

These expressions are plotted along with results from quantum Monte Carlo using worm updates (to be discussed in detail below) in Fig. 5.3.

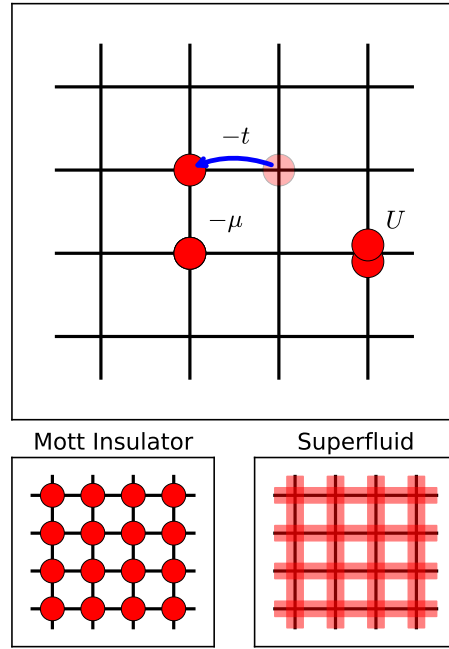


**Figure 5.1:** Illustration of a BH model on a two-dimensional square lattice. In the Mott insulator phase, the particles are localized to a site, and in the superfluid phase the particles can *wind* across the system.

### Partition function

A problem of statistical mechanics is to calculate the partition function, that is calculating the trace of  $e^{-\beta H}$ , a task most straightforwardly written as

$$Z = \sum_{\alpha_n} \langle \alpha_n | e^{-\beta H} | \alpha_n \rangle \quad (5.5a)$$

$$= \sum_i e^{-\beta E_i}, \quad (5.5b)$$

where the  $|\alpha_n\rangle$  is a complete orthonormal set and  $E_i$  the energy eigenvalues of  $H$ . In this form, it is necessary to determine the eigenvalues  $E_i$  of the Hamiltonian operator, and then carry out the sum over all corresponding

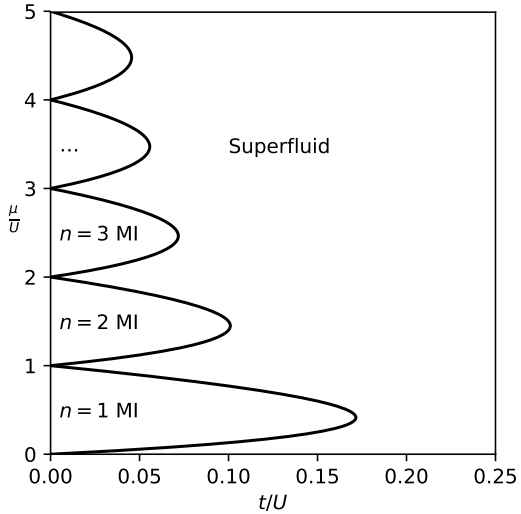


**Figure 5.2:** A mean-field phase diagram for a one-dimensional Bose-Hubbard model given by  $t_c/U = (n - \mu/U)(\mu/U - n + 1)/(\mu/U + 1)$ , see e.g. [126].

weights  $e^{-\beta E_i}$ , as Feynman put it [132] a “hopelessly difficult” calculation. Instead we reformulate the problem in terms of imaginary time path integrals [132, 69, 133].

### Imaginary-time path integral reformulation of the partition function

First, we outline the reformulation of (5.5) in terms of path integrals, with the Bose-Hubbard model (5.2) in mind. Following the derivation in [69], first denote the statistical operator

$$\rho(\beta) = e^{-\beta H}. \quad (5.6)$$

It then follows that

$$\frac{\partial \rho}{\partial \beta} = -H\rho, \quad (5.7)$$

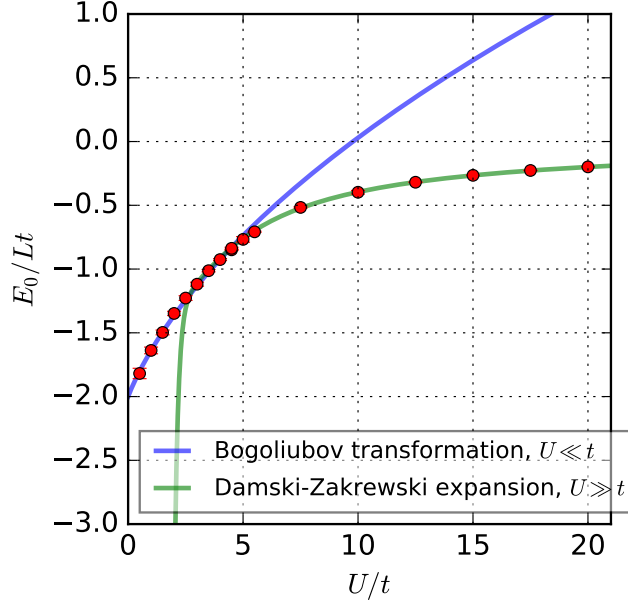


**Figure 5.3:** Ground state energy of a one-dimensional BH model at unity filling factor. Solid blue line: Eq. (5.3). Solid green line: Eq. (5.4). The red dots correspond to worm quantum Monte Carlo simulations with  $L = 10$  and  $\beta = 100/t$ .

with the condition  $\rho(0) = 1$ . Let now  $H = K + V$  (kinetic and potential energy), from (5.7) it then follows that

$$\frac{\partial}{\partial \beta} (e^{\beta V} \rho) = V e^{\beta V} \rho + e^{\beta V} \partial_\beta \rho \quad (5.8a)$$

$$= V e^{\beta V} \rho - e^{\beta V} H \rho \quad (5.8b)$$

$$= -e^{\beta V} K \rho. \quad (5.8c)$$

Integrating from 0 to  $\beta$  and rearranging terms gives

$$\rho(\beta) = e^{-\beta V} \left( 1 - \int_0^\beta d\tau_1 e^{\tau_1 V} K \rho(\tau_1) \right), \quad (5.9)$$

where we have introduced the integration variable  $\tau_1$ , corresponding to imaginary time. By repeatedly inserting (5.9) into itself and denoting  $K(\tau) =$

$e^{\tau V} K e^{-\tau V}$ , a series is obtained:

$$e^{-\beta H} = e^{-\beta V} \left( 1 - \int_0^\beta d\tau_1 K(\tau_1) \right) \quad (5.10a)$$

$$+ \int_0^\beta d\tau_1 \int_0^{\tau_1} d\tau_2 K(\tau_1) K(\tau_2) \quad (5.10b)$$

$$- \int_0^\beta d\tau_1 \int_0^{\tau_1} d\tau_2 \int_0^{\tau_2} d\tau_3 K(\tau_1) K(\tau_2) K(\tau_3) \quad (5.10c)$$

$$+ \dots \right). \quad (5.10d)$$

In the series (5.10) we have integrands of the form (see e.g. [51])

$$O_n \equiv e^{-(\beta-\tau_1)V} K e^{-(\tau_1-\tau_2)V} K e^{-(\tau_2-\tau_3)V} \dots \\ \dots e^{-(\tau_{n-2}-\tau_{n-1})V} K e^{-(\tau_{n-1}-\tau_n)V} K e^{-\tau_n V}. \quad (5.11)$$

Let these terms operate on state vectors  $|\alpha\rangle = |n_1, n_2, \dots\rangle$  in the Fock basis:

$$V|\alpha_m\rangle = V_{\alpha_m}|\alpha_m\rangle, \quad (5.12a)$$

$$K|\alpha_m\rangle = \sum_{\alpha_n} K_{\alpha_n}^{\alpha_m} |\alpha_n\rangle, \quad (5.12b)$$

$$K_{\alpha_m}^{\alpha_m} = 0, \quad (5.12c)$$

where  $n$  and  $m$  are indices which enumerate Fock basis states.

The expectation values of the terms  $O_n$  in the series with respect to a state  $|\alpha_n\rangle$  then become

$$\langle \alpha_n | O_n | \alpha_n \rangle = \sum_{\{\alpha_k\}_{k=1}^{n-1}} K_{\alpha_n}^{\alpha_1} K_{\alpha_1}^{\alpha_2} \dots K_{\alpha_{n-2}}^{\alpha_{n-1}} K_{\alpha_{n-1}}^{\alpha_n} \exp \left\{ - \int_0^\beta d\tau V[\alpha(\tau)] \right\}. \quad (5.13)$$

Finally, according to (5.5a) the partition function becomes

$$Z = \sum_{n=0}^{\infty} \sum_{\{\alpha_k\}_{k=1}^n} \int_0^\beta \int_0^{\tau_1} \dots \int_0^{\tau_n} (-1)^n d^n \tau \prod_{j=1}^n K_{\alpha_{j-1}}^{\alpha_j} \exp \left\{ - \int_0^\beta d\tau V[\alpha(\tau)] \right\}, \quad (5.14)$$

where  $d^n \tau = d\tau_1 d\tau_2 \dots d\tau_n$ .

### Partition function for the BH model

The partition function of the form (5.14) looks like a mess, but it can nevertheless be attempted to sample it using Monte Carlo integration. The

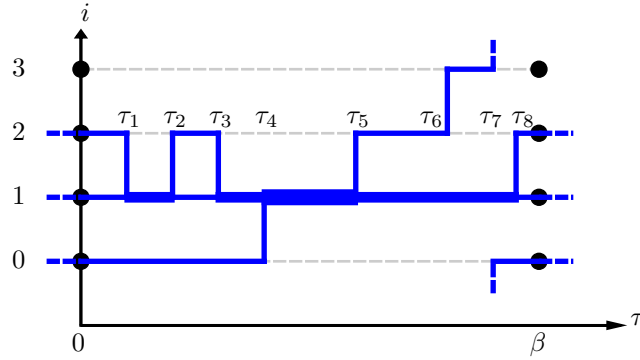


**Figure 5.4:** An example of a possible worldline configuration with a one-dimensional periodic lattice with four sites  $i = 0, 1, 2, 3$ , and eight transition times between 0 and  $\beta$  on the imaginary time  $\tau$ -axis. The system is periodic on both axes. The thickness of the blue line corresponds to the number of particles.

integrand of (5.14) can now be seen as a weight function, summed over all closed paths. If we abbreviate the closed path summation as  $\sum_{c.p.}$  we can write

$$Z = \sum_{c.p.} W, \quad (5.15a)$$

$$W = (-1)^n d^n \tau \prod_{j=1}^n K_{\alpha_{j-1}}^{\alpha_j} \exp \left\{ - \int_0^\beta d\tau V[\alpha(\tau)] \right\}. \quad (5.15b)$$

A configuration can be pictorially represented as a lattice path integral, for example of the form illustrated in Fig. 5.4. The path integral sums all possible paths for an initial state  $|\alpha\rangle$  propagating in spacetime to finally return to itself after a time  $\beta$  (so that  $|\alpha(0)\rangle = |\alpha(\beta)\rangle$ ), and the partition function is obtained by summing over all initial states  $|\alpha\rangle$ . Using the Metropolis algorithm we can estimate thermal expectation values of observables by arithmetic averaging from configurations generated with probabilities according to the weight function  $W$ .

In Fig. 5.4 an example configuration is illustrated where the particle number depends on one spatial variable and imaginary time. In this particular example there are four sites and periodic boundary conditions are applied. The particle trajectories are called *worldlines*. The state

$$|\alpha(\tau)\rangle = |n_0(\tau), n_1(\tau), n_2(\tau), n_3(\tau)\rangle$$

where  $n_i(\tau)$  is the number of particles on site  $i$  at time  $\tau$ . For the example in Fig. 5.4 we have

$$|\alpha(\tau)\rangle = \begin{cases} |1,1,1,0\rangle & \text{if } 0 < \tau < \tau_1 \\ |1,2,0,0\rangle & \text{if } \tau_1 < \tau < \tau_2 \\ |1,1,1,0\rangle & \text{if } \tau_2 < \tau < \tau_3 \\ |1,2,0,0\rangle & \text{if } \tau_3 < \tau < \tau_4 \\ |0,3,0,0\rangle & \text{if } \tau_4 < \tau < \tau_5 \\ |0,2,1,0\rangle & \text{if } \tau_5 < \tau < \tau_6 \\ |0,2,0,1\rangle & \text{if } \tau_6 < \tau < \tau_7 \\ |1,2,0,0\rangle & \text{if } \tau_7 < \tau < \tau_8 \\ |1,1,1,0\rangle & \text{if } \tau_8 < \tau < \beta \end{cases} \quad (5.16)$$

where it can be noted that  $|\alpha(0)\rangle = |\alpha(\beta)\rangle$  and that the system is periodic in the spatial dimension. It can also be noted in Fig. 5.4 that one particle *winds* over the spatial extent of the system when propagating from 0 to  $\beta$  in imaginary time. This gives a non-zero *winding number*  $W = +1$ , which contributes statistically to a superfluid density with the Pollock-Ceperley formula [77] (see paper 5 for details of this formula for the multi-species case).

For a given set of model parameters  $U/t$ ,  $\mu/t$  and  $\beta$ , the weight function  $W$  for this particular configuration is then a number that can be calculated from (5.15b). The numerical values of the terms  $K_{\alpha_{j-1}}^{\alpha_j}$  follow from basic second quantization identities for bosons (see e.g. [134])

$$b_i|n_i\rangle = \sqrt{n_i}|n_i - 1\rangle, \quad (5.17a)$$

$$b_i^\dagger|n_i\rangle = \sqrt{n_i + 1}|n_i + 1\rangle. \quad (5.17b)$$

Let  $|\alpha_m\rangle = |n_1, \dots, n_i, \dots, n_j, \dots\rangle$ , with the Bose-Hubbard model in mind we have

$$b_j^\dagger b_i|n_1, \dots, n_i, \dots, n_j, \dots\rangle = b_j^\dagger \sqrt{n_i}|n_1, \dots, n_i - 1, \dots, n_j, \dots\rangle \quad (5.18a)$$

$$= \sqrt{n_i(n_j + 1)}|n_1, \dots, n_i - 1, \dots, n_j + 1, \dots\rangle. \quad (5.18b)$$

If  $|\alpha_n\rangle = |n_1, \dots, n_i - 1, \dots, n_j + 1, \dots\rangle$  we then have

$$K_{\alpha_n}^{\alpha_m} = \langle \alpha_n | K | \alpha_m \rangle = -t \sqrt{n_i(n_j + 1)}. \quad (5.19)$$

Furthermore, for reasons to become apparent, we consider contributions from worldline discontinuities (where the particle number is not conserved) of ‘strength’  $\eta$ . With  $|\alpha_n\rangle = |n_1, \dots, n_i - 1, \dots\rangle$  and  $|\alpha'_n\rangle = |n_1, \dots, n_j + 1, \dots\rangle$

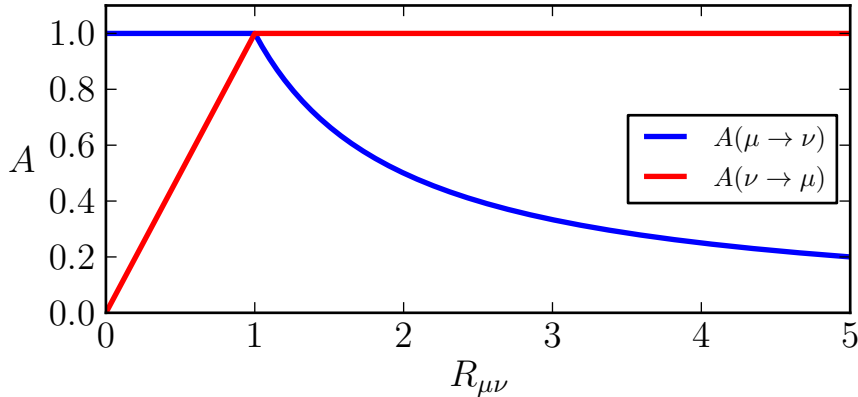


**Figure 5.5:** Acceptance probabilities (5.24) that form a correct acceptance ratio  $R_{\mu\nu}$ .

such terms take the values

$$\langle \alpha_n | \eta b_i | \alpha_m \rangle = \eta \sqrt{n_i}, \quad (5.20a)$$

$$\langle \alpha'_n | \eta b_j^\dagger | \alpha_m \rangle = \eta \sqrt{n_j + 1}. \quad (5.20b)$$

We are now ready to discuss the Monte Carlo sampling of the BH model.

## 5.2 Quantum Monte Carlo for the BH model

In what follows, we will consider a square lattice in  $d$  dimensions with on-site interactions only.

### Detailed balance revisited

In Ch. 2.3 we discussed detailed balance, and assumed that the *proposal distributions* are symmetric. If the proposal distributions are not symmetric, they do not automatically cancel in the detailed balance equation. The detailed balance equation is

$$W_\mu P(\mu \rightarrow \nu) = W_\nu P(\nu \rightarrow \mu), \quad (5.21)$$

where  $W_\mu$  is the configuration weight for the state  $\mu$  and as usual the transition probability distribution  $P$  can be decomposed into a proposal distribution  $g$  and an acceptance distribution  $A$  (see e.g. [86]):

$$P(\mu \rightarrow \nu) = g(\mu \rightarrow \nu) A(\mu \rightarrow \nu). \quad (5.22)$$

Let the *acceptance ratio*  $R_{\mu\nu}$  for a  $\mu \rightarrow \nu$  transition be

$$R_{\mu\nu} \equiv \frac{A(\nu \rightarrow \mu)}{A(\mu \rightarrow \nu)} = \frac{W_\mu g(\mu \rightarrow \nu)}{W_\nu g(\nu \rightarrow \mu)}. \quad (5.23)$$

Clearly,  $R_{\mu\nu} = R_{\nu\mu}^{-1}$ . When a state  $\nu$  has been suggested from  $\mu$  or vice versa with the proposal distributions  $g(\mu \rightarrow \nu)$  and  $g(\nu \rightarrow \mu)$ , the acceptance ratio is some number which is calculated from the right-hand side of (5.23). To ensure detailed balance, we choose the acceptance probabilities such that the ratio  $A(\nu \rightarrow \mu)/A(\mu \rightarrow \nu)$  equals this number  $W_\mu g(\mu \rightarrow \nu)/(g(\nu \rightarrow \mu)W_\nu)$ . For example we can let (see Fig. 5.5)

$$A(\mu \rightarrow \nu) = \begin{cases} 1/R_{\mu\nu} & \text{if } R_{\mu\nu} > 1 \\ 1 & \text{otherwise} \end{cases} \quad (5.24a)$$

$$A(\nu \rightarrow \mu) = \begin{cases} 1 & \text{if } R_{\mu\nu} > 1 \\ R_{\mu\nu} & \text{otherwise} \end{cases} \quad (5.24b)$$

which are between zero and one and form a correct acceptance ratio. During a simulation, we draw a random number between zero and one, and if it is less than  $A$ , the proposed move is accepted.

### Measuring the energy

From (5.15) we obtain the ensemble average potential energy  $V$

$$\langle V \rangle = \frac{\sum_{c.p.} V_{c.p.} W}{\sum_{c.p.} W}, \quad (5.25)$$

where  $V_{c.p.}$  is the configuration-averaged potential energy for a particular closed path,

$$V_{c.p.} = \frac{1}{\beta} \int_0^\beta d\tau V[\alpha(\tau)]. \quad (5.26)$$

Supposing we have generated  $N$  samples of  $V_{c.p.}$ , all with probabilities proportional to their weights  $W$ , the Monte Carlo estimator becomes

$$\langle V \rangle_{MC} = \frac{1}{N} \sum V_{c.p..} \quad (5.27)$$

The kinetic energy  $K = -t \sum_{\langle ij \rangle} b_i^\dagger b_j$  can be calculated by counting the number of kinks  $N_{kinks}$  in the sampled configurations, the ensemble average of

$K$  is

$$\langle K \rangle = \frac{1}{Z} \text{Tr} [Ke^{-\beta(V+K)}] \quad (5.28a)$$

$$= \frac{1}{Z} \text{Tr} \left[ -\frac{t}{\beta} \frac{\partial}{\partial t} e^{-\beta(V+K)} \right] \quad (5.28b)$$

$$= -\frac{t}{\beta} \frac{1}{Z} \frac{\partial Z}{\partial t}. \quad (5.28c)$$

Since the configuration weight (5.15) is proportional to  $t^{N_{kinks}}$ , we can write

$$Z = \sum_{c.p.} W \quad (5.29a)$$

$$= \sum_{c.p.} W_0 t^{N_{kinks}}, \quad (5.29b)$$

where  $W_0$  is independent of  $t$ . Then,

$$\langle K \rangle = -\frac{t}{\beta} \frac{\sum_{c.p.} W_0 N_{kinks} t^{N_{kinks}-1}}{\sum_{c.p.} W} \quad (5.30a)$$

$$= -\frac{1}{\beta} \frac{\sum_{c.p.} N_{kinks} W}{\sum_{c.p.} W} \quad (5.30b)$$

$$= -\frac{\langle N_{kinks} \rangle}{\beta}, \quad (5.30c)$$

where  $\langle N_{kinks} \rangle$  is the ensemble average of the number of kinks. With  $N$  samples of  $N_{kinks}$  from configurations sampled by their configuration weights we have

$$\langle K \rangle_{MC} = -\frac{1}{\beta N} \sum N_{kinks}. \quad (5.31)$$

### 5.3 Worm algorithm for the BH model

Early quantum Monte Carlo simulations of the Bose-Hubbard model, e.g. [127], used local updates of the configuration space such that the sampled configurations always had the same winding number. This issue was resolved with the worm algorithm [78, 79], see also [51, 135, 136, 137]. Worm updates have multiple advantages listed in [79], where the most important ones for our purposes is that worm updates can ease critical slowing-down and are not restricted to the zero winding number sector.

Loosely speaking, the algorithm consists of extending the configuration space by considering worldline paths with discontinuities, like a broken string, called a worm. The worm end(s) then moves through the system

by a set of extended configuration space updates, and can be removed or closed, creating a new regular configuration, which can be sampled. In Fig. 5.6 we show illustrative examples of configurations in one dimension obtained from simulations with worm updates. Some configurations are from the extended configuration space where the worm head is shown by a filled circle and the tail by a crossed circle. In case the tail is not visible, it is covered by the head. For the figures corresponding to large  $t$ , the transitions visible consist of a particle jumping to a site and jumping back very shortly thereafter, and such appear as single lines although they consist of two transitions.

### **Worm creation and destruction**

The creation and destruction of a worm is an update-antiupdate pair. We can design the worm creation procedure as follows. Let  $\mu$  be a worm-less system, see Fig. 5.7, a worm creation trial move will then be attempted with probability  $p_c = 1$ , which contributes a factor  $p_c$  to  $g(\mu \rightarrow \nu)$  (for clarity, we will explicitly write out  $p_c$  although it is always equal to one). Let  $N$  be the number of intervals with a constant  $n$  (not double counting intervals that cross the periodic  $\beta$ -boundary, and not forgetting intervals with  $n = 0$ ).

Let the  $g(\mu \rightarrow \nu)$  distribution be designed by the following. In this sequence of steps we have contributions to  $g(\mu \rightarrow \nu)$  by the factors  $p_c$  (the probability of making a creation update),  $1/N$  (selection of an interval),  $(d\tau/(\tau_{max} - \tau_{min}))^2$  (generation of times for the head and tail, with  $\tau_{max} - \tau_{min} = \beta$  if the selected interval is without kinks in time). Note that our construction where the worm is inserted on an interval where the particle number  $n$  is fixed, is for the purpose of easily determining the configuration weight  $W_\mu/W_\nu$ , to be done below.

The proposal distribution between a wormless configuration  $\mu$  to a configuration  $\nu$ , where a worm is inserted, is therefore:

$$g(\mu \rightarrow \nu) = p_c \times \frac{1}{N} \times \frac{(d\tau)^2}{(\tau_{max} - \tau_{min})^2} \left( \times \frac{1}{2} \right), \quad (5.32)$$

where the last factor occurs only for the special case with a kink-less site.

The worm destruction scheme is devised as follows. If we are in the  $\nu$  with a worm, we suggest with probability  $p_d < 1$  to destroy the worm, i.e. suggest the state  $\mu$ . The only other factor that contributes to  $g(\nu \rightarrow \mu)$  is the factor  $1/2$  that may occur when deleting a worm on an otherwise empty site (except for completely flat intervals). Thus the proposal distribution for worm destruction is

$$g(\nu \rightarrow \mu) = p_d \left( \times \frac{1}{2} \right), \quad (5.33)$$

where, as for creation, the last term is due to the special case with a kink-less site. Luckily, these factors ( $1/2$  in (5.32) and (5.33)) cancel in the

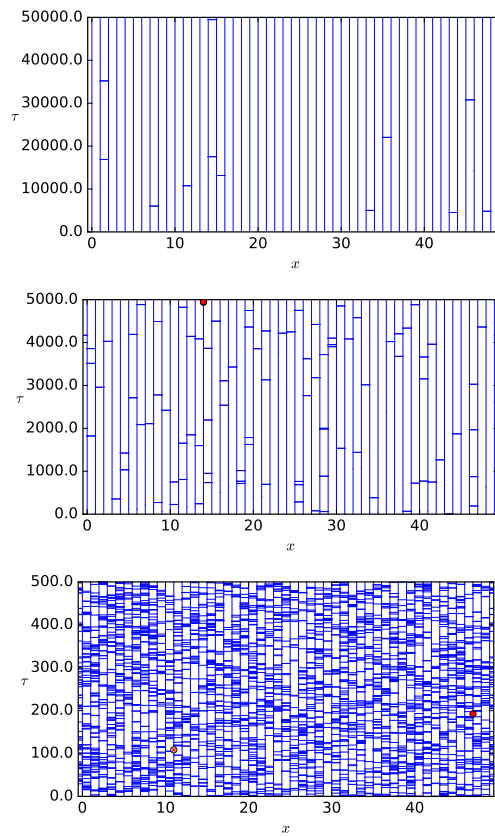


**Figure 5.6:** Configurations obtained after 100 million worm updates per site for a one-dimensional one-component BH-model. The horizontal  $x$ -axis is the site index, and the vertical  $\tau$  axis is imaginary time. Periodic boundary conditions are imposed on the  $x$ -axis, and the  $\tau$ -axis is  $\beta$ -periodic. Here  $L = 50$ ,  $U = 1.0$ ,  $\beta = L/t$ ,  $\mu = 0.75$  and  $t$  is, from above to below, 0.001, 0.01, and 0.1 respectively.

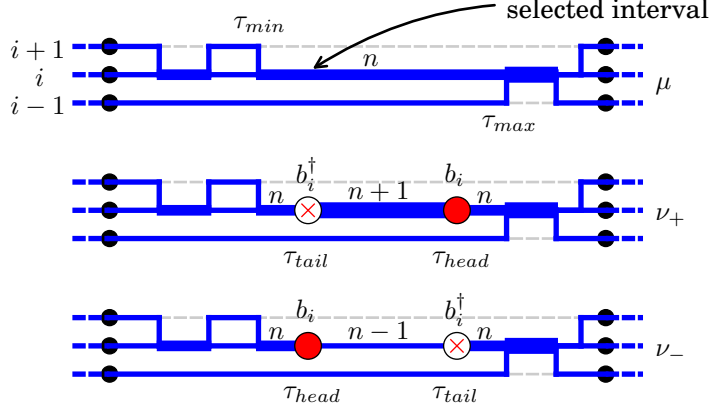


**Figure 5.7:** Illustration of worm creation ( $\mu \rightarrow \nu$ ) and deletion ( $\nu \rightarrow \mu$ ). Starting from the wormless state  $\mu$ , one of the flat intervals is selected at random and  $\tau_{head}$  and  $\tau_{tail}$  are generated within the time limits of the interval. If  $\tau_{head} > \tau_{tail}$  a worm is added on top of the interval (as in  $\nu_+$ ). If instead  $\tau_{head} < \tau_{tail}$  we select randomly one of the worldlines constituting the selected flat trajectory and turn it into a worm (as in  $\nu_-$ ). A special case occurs if the chosen interval is a flat interval from 0 to  $\beta$ .

acceptance ratio. The configuration weight ratios  $W_\mu/W_{\nu_+}$  (when  $\tau_{head} > \tau_{tail}$ ) and  $W_\mu/W_{\nu_-}$  (when  $\tau_{tail} > \tau_{head}$ ) can be obtained from (5.15b) and (5.20)

$$\frac{W_\mu}{W_{\nu_+}} = \frac{1}{\eta^2(n+1)(d\tau)^2} \exp\left(-(\tau_{head} - \tau_{tail})\left(-\frac{U}{2}(2n+1) + \mu\right)\right), \quad (5.34a)$$

$$\frac{W_\mu}{W_{\nu_-}} = \frac{1}{\eta^2 n(d\tau)^2} \exp\left(-(\tau_{tail} - \tau_{head})\left(-\frac{U}{2}(-2n+1) - \mu\right)\right). \quad (5.34b)$$

The denominators in (5.34) come from the worldline discontinuities due to the worm head and tails, as determined from (5.20). For  $W_{\nu_+}$  the worldline discontinuity terms are  $b_i|n_i+1\rangle = \sqrt{n_i+1}|n_i\rangle$  and  $b_i^\dagger|n_i\rangle = \sqrt{n_i+1}|n_i+1\rangle$ , which gives the factor  $n_i+1$  to  $W_{\nu_+}$ . For  $W_{\nu_-}$ , they are  $b^\dagger|n_i-1\rangle = \sqrt{n_i-1+1}|n_i\rangle$  and  $b|n_i\rangle = \sqrt{n_i}|n_i-1\rangle$ , which gives the factor  $n_i$  to  $W_{\nu_-}$ . The probability that a worm is present at a given time in a simulation will depend on the term  $\eta^2$ .

The acceptance ratio (5.23) for worm creation according to this scheme then becomes

$$R_{\mu\nu} = \frac{g(\mu \rightarrow \nu)}{g(\nu \rightarrow \mu)} = (d\tau)^2 \frac{W_\mu}{W_{\nu_\pm}} \frac{p_c}{p_d N(\tau_{max} - \tau_{min})^2}, \quad (5.35)$$

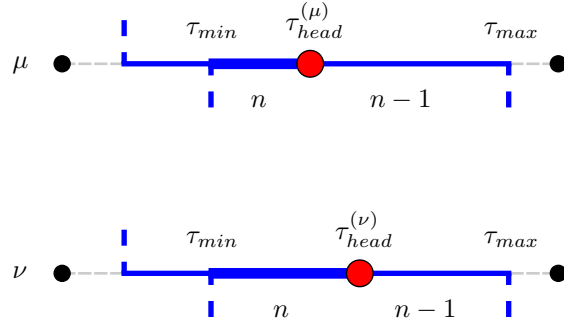


**Figure 5.8:** Illustration of the time shift update.

where, again,  $\mu$  is the wormless state and  $\nu$  is the worm-inserted state.

### Time shift

In the time shift update, which is illustrated in Fig. 5.8 and is attempted with probability  $p_{ts}$ , the time of the wormhead is randomly updated to a time within the interval  $(\tau_{min}, \tau_{max})$ . A straightforward calculation gives the configuration weight ratio for such a move as

$$\frac{W_\mu}{W_\nu} = \exp \left[ - \left( \tau_{head}^{(\mu)} - \tau_{head}^{(\nu)} \right) \left( \frac{U}{2} (2n - 1) - \mu \right) \right]. \quad (5.36)$$

Since the worldline discontinuity stays in between the same intervals, contributions with  $\eta$  cancel in (5.36). We can use symmetric proposal distributions

$$g(\mu \rightarrow \nu) = p_{ts} \times \frac{d\tau}{\tau_{max} - \tau_{min}}, \quad (5.37a)$$

$$g(\nu \rightarrow \mu) = g(\mu \rightarrow \nu), \quad (5.37b)$$

so the acceptance ratio (5.23) for time shift is simply

$$R_{\mu\nu} = \frac{W_\mu}{W_\nu} \frac{g(\mu \rightarrow \nu)}{g(\nu \rightarrow \mu)} = \frac{W_\mu}{W_\nu}, \quad (5.38)$$

where the right-hand side is given by (5.36).

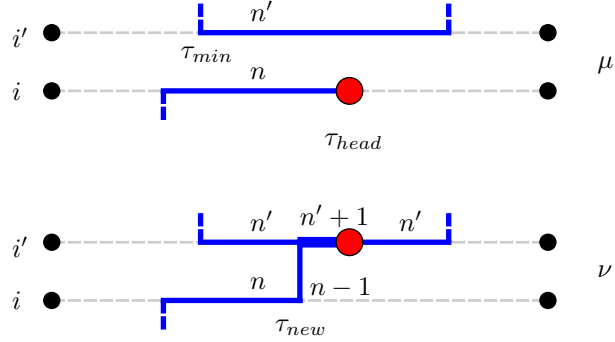


**Figure 5.9:** Illustration of the jump update ( $\mu \rightarrow \nu$ ) and the anti-jump update ( $\nu \rightarrow \mu$ ).

### Jump and anti-jump

In the jump update, which is illustrated in Fig. 5.9 and is attempted with probability  $p_j$  (and anti-jump is performed with probability  $p_{aj}$ ), the worm-head is displaced to a neighboring site  $i'$ , while the time of the wormhead is unchanged. Assuming a rectangular lattice, one of the  $2d$  spatial directions are chosen randomly giving a factor of  $1/(2d)$  to  $g$ . A kink is inserted at a random  $\tau_{new}$  in  $(\tau_{min}, \tau_{head})$ , giving a factor  $d\tau/(\tau_{head} - \tau_{min})$  to  $g$ . The kink insertion changes the kinetic energy of the configuration according to  $-tb_{i'}^\dagger b_i |n, n'\rangle = -t\sqrt{n(n'+1)}|n-1, n'+1\rangle$ , giving

$$W_\nu \propto t\sqrt{n(n'+1)}. \quad (5.39)$$

This is partially compensated by the change in configuration weight due to the head. In the state  $\mu$  we have  $\eta b_i |n\rangle = \eta\sqrt{n}|n-1\rangle$  and in  $\nu$  we have  $\eta b_{i'} |n'+1\rangle = \eta\sqrt{n'+1}|n'\rangle$  such that

$$W_\mu \propto \eta\sqrt{n}, \quad (5.40a)$$

$$W_\nu \propto \eta\sqrt{n'+1}. \quad (5.40b)$$

The configuration weight ratio then becomes

$$\frac{W_\mu}{W_\nu} = \frac{1}{t(n'+1)d\tau} \exp [-(\tau_{head} - \tau_{new})U(n - n' - 1)], \quad (5.41)$$

where the first factor is due to the change of the head worldline discontinuity and the kinetic energy, and the exponential factor is due to the potential

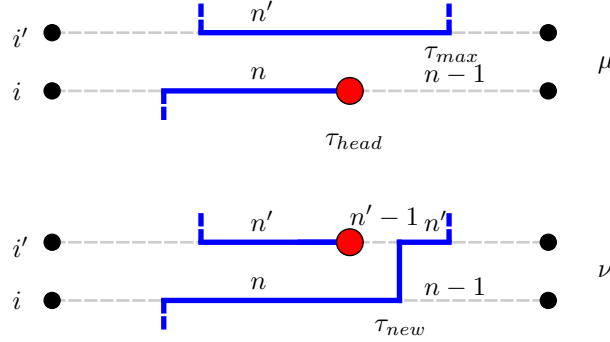


**Figure 5.10:** Illustration of the reconnection update ( $\mu \rightarrow \nu$ ) and the anti-reconnection update ( $\nu \rightarrow \mu$ ).

energy. The proposal distributions for jump and anti-jump become

$$g(\mu \rightarrow \nu) = p_j \times \frac{1}{2d} \times \frac{d\tau}{(\tau_{head} - \tau_{min})}, \quad (5.42a)$$

$$g(\nu \rightarrow \mu) = p_{aj}, \quad (5.42b)$$

giving the acceptance ratio

$$R_{\mu\nu} = \frac{W_\mu}{W_\nu} \frac{g(\mu \rightarrow \nu)}{g(\nu \rightarrow \mu)} = \frac{p_j \exp [-(\tau_{head} - \tau_{new})U(n - n' - 1)]}{2dp_{aj}(n' + 1)t(\tau_{head} - \tau_{min})}. \quad (5.43)$$

### Reconnection and anti-reconnection

The final update is the reconnection update and is illustrated in Fig. 5.10. With probability  $p_{rc}$  the worm is suggested to reconnect with an existing trajectory, and the inverse move is attempted with probability  $p_{arc}$ . The configuration weight ratio becomes

$$\frac{W_\mu}{W_\nu} = \sqrt{\frac{n}{n'}} \frac{1}{t\sqrt{nn'd\tau}} \exp [-(\tau_{new} - \tau_{head})U(n' - n)]. \quad (5.44)$$

The proposal distribution for the  $\mu \rightarrow \nu$  update has a factor  $p_{rc}$ , a factor  $2d$  (as for the jump update one out of  $2d$  directions are chosen randomly) and a  $\tau_{new}$  is generated from a uniform distribution giving the factor  $d\tau/(\tau_{max} - \tau_{head})$ , so that

$$g(\mu \rightarrow \nu) = p_{rc} \times \frac{1}{2d} \times \frac{d\tau}{(\tau_{max} - \tau_{head})}, \quad (5.45)$$

and the distribution for the  $\nu \rightarrow \mu$  update is simply

$$g(\nu \rightarrow \mu) = p_{arc}. \quad (5.46)$$

Note that  $\tau_{max}$  may be set by some kink belonging to some other interval on either of the sites  $i$  or  $i'$ . Thus we get the acceptance ratio

$$R_{\mu\nu} = \frac{W_\mu}{W_\nu} \frac{g(\mu \rightarrow \nu)}{g(\nu \rightarrow \mu)} = \frac{p_{rc} \exp [-(\tau_{new} - \tau_{head})U(n' - n)]}{p_{arc} 2d(\tau_{max} - \tau_{head})tn'}. \quad (5.47)$$

This finalizes our description of the Monte Carlo moves of a worm algorithm.

#### 5.4 Two-component Bose-Hubbard model and calculated drag interaction

For a two-component BH model with components  $a$  and  $b$ , interspecies interactions must be included. A simple interaction as an on-site interspecies interaction  $U_{ab}$  so that the Hamiltonian is given by

$$H = H_a + H_b + U_{ab} \sum_i n_i^{(a)} n_i^{(b)}. \quad (5.48)$$

where  $H_a = -t_a \sum_{\langle ij \rangle} c_i^{(a)\dagger} c_j^{(a)} + (U_a/2) \sum_i n_i^{(a)} (n_i^{(a)} - 1) - \mu_a \sum_i n_i^{(a)}$ , i.e. the one-component BH Hamiltonian (5.2) with labels for  $a$ , and  $H_b$  defined analogously. The term  $U_{ab}$  is an interspecies on-site interaction which may be either repulsive or attractive. A superfluid drag interaction can be induced by  $U_{ab}$ , see Fig. 5.11. For details, refer to paper 5. In particular, *paired phases* where the drag saturates to its maximal value are observed in paper 5.

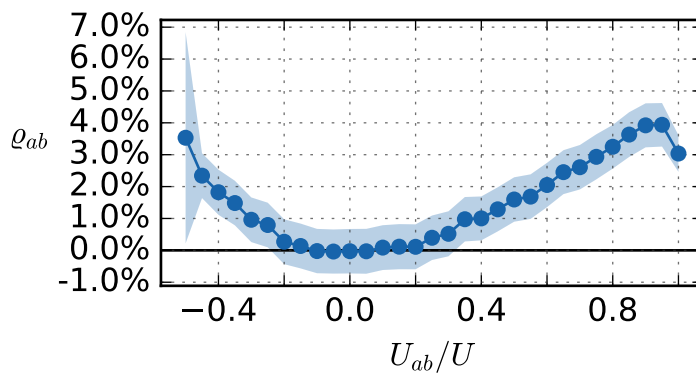


**Figure 5.11:** Results for the drag interaction, expressed a fraction of the one-species superfluid densities, obtained from worm quantum Monte Carlo for a two-component two-dimensional square-lattice BH model with  $U_a = U_b = U = 1$ ,  $t_a = t_b = t = 0.1$ ,  $\beta = 1000$ ,  $L = 10$  and the chemical potential is adjusted to keep the total filling factor close to 0.5.



## **Chapter 6**

# **Conclusions and outlook**

Multicomponent superconductors and superfluids possess a much richer variety of phenomena than one-component systems. In this thesis, a number of examples have been considered. It has been demonstrated that vortices in multicomponent systems can have a plethora of structural phases, due to complicated interactions which in turn are due to multicomponent effects. Topological defects have, in turn, connections to phase transitions. By a Peskin-Dasgupta-Halperin duality, one-component  $U(1)$  London lattice superconductors have a continuous “inverted-3DXY” phase transition. However, it has been shown in this thesis that the phase transition of multicomponent  $U(1)$  London lattice superconductors can be first-order, which was interpreted as a fluctuation-induced attraction between vortices. A similar effect can occur in superfluids due to an intercomponent drag effect, which is believed to play an important role in multicomponent systems. It was shown in this thesis that the drag interaction can lead to stabilization of skyrmions in two-component superconductors, when composite vortices core-split and phase separate in the ground state. Lastly, the microscopic emergence of a drag interaction in a two-species Bose-Hubbard model was considered. A substantial drag was found even in the case of on-site boson-boson interactions, and paired phases where the drag saturates to maximal values were observed.

Certainly many questions within the field of multicomponent superconductors and superfluids remain unanswered. However, in a more broad context, this thesis is an example of a modern way of conducting theoretical physics research with supercomputer calculations, made possible by recent technological developments. For example, Onsager suggested the “*vortex-loop blowout*” scenario already in 1949, but a quantitative analysis of such a scenario was hardly possible back then [50]. For an outlook of future research directions, it is thus interesting to discuss the current and future relation of theoretical physics research with technology, more

specifically computers and algorithms.

Technology has always been advanced by basic physics research. For example, there was thermodynamics and later refrigerators, electrodynamics and later antennas, quantum mechanics and later transistors. Conversely, basic physics research has been advanced by technology. There is thus a synergy between technology and physics, as advancements in technology lead to more powerful tools such as supercomputers and sophisticated experimental equipment, which lead to advancements in physics. As technology and physics develop, so seems the complexity of the problems that arise. The development of technology seem to require increasingly sophisticated innovation, and physics research seem to require increasingly powerful equipment. Computing hardware power has in recent decades become abundant, however, good software is needed to put the hardware to good use. It can be particularly difficult to numerically simulate quantum systems composed of many particles. For a classical Newtonian system, the equations of motion governing the positions of a set of  $N$  classical particles is a system of  $N$  coupled differential equations, which can be a relatively straightforward task for a computer to solve numerically. On the other hand, the corresponding equation of motion for the  $N$ -particle quantum problem is given by the many-body Schrödinger equation, which is *one* equation, but of  $N$  variables! Representing this equation in computer memory, for even moderately large  $N$ , becomes a hopelessly difficult task for a classical computer, let alone solving the equation.

One specialized technique that can solve some quantum many-body problems is *path-integral Monte Carlo* simulations that have been discussed in this thesis. There, the celebrated Feynman path-integral formulation of quantum mechanics [138, 74] is used instead of the Schrödinger equation. This allows one to write the problem as a complicated series of integrals instead of a complicated differential equation. The beauty of this is that complicated high-dimensional integrals can be calculated (somewhat generically) using Monte Carlo integration, a numerically exact stochastic sampling technique using random numbers [83]. For some bosonic systems this method has had enormous success, leading to computer codes capable of more or less exactly simulating some very complicated quantum systems like superfluid helium models [76] or lattice boson models [79].

Particles are typically grouped into fermions and bosons. Unfortunately, simulating fermions with path-integral Monte Carlo can be difficult since the method can break down catastrophically due to the fermion sign problem [139]. This is unfortunate since many interesting problems are fermionic. In short, a sign problem can occur when the series of the integrals in the path-integral formulation come with different signs. The answer, if expressed as a series of terms which are similar in magnitude but opposite in sign, can then converge impractically slowly. The relative error of the answer can furthermore diverge in the thermodynamic limit [140].

Recently, *diagrammatic Monte Carlo* [141, 142, 143, 144] techniques has had some progress in the simulation of fermion systems. Rather than working in the path-integral formulation, the problem can be written in the thermodynamic limit in terms of a series of Feynman diagrams, which is then sampled stochastically. Another approach is to “simulate” quantum systems with ultracold quantum gases [145, 146]. Even more recently, artificial intelligence and machine learning techniques have been applied to many-body quantum physics. Recent works with machine learning have been to estimate the energy levels of many-body quantum problems [147], as well as applications for the fermion sign problem [148, 149], and more [150, 151, 152]. Ultimately, the computational complexities of quantum physics can perhaps only be resolved with quantum computers [153]. Such devices will likely lead to enormous technological and scientific impact.



# Bibliography

- [1] L. Onsager. Statistical hydrodynamics. *Il Nuovo Cimento (1943-1954)*, 6(2):279–287, Mar 1949. <http://dx.doi.org/10.1007/BF02780991>.
- [2] R.P. Feynman. Application of quantum mechanics to liquid helium, 1955. [https://doi.org/10.1016/S0079-6417\(08\)60077-3](https://doi.org/10.1016/S0079-6417(08)60077-3).
- [3] A. A. Abrikosov. Magnetic properties of superconductors of the second group. *Soviet Physics JETP*, 5(6):1174–1182, 1957. <http://www.jetp.ac.ru/cgi-bin/e/index/e/5/6/p1174?a=list>.
- [4] V. L. Berezinskii. Destruction of Long-range Order in One-dimensional and Two-dimensional Systems having a Continuous Symmetry Group I. Classical Systems. *Soviet Physics JETP*, 32(3):493–500, 1971. <http://www.jetp.ac.ru/cgi-bin/e/index/e/32/3/p493?a=list>.
- [5] J. M. Kosterlitz and D. J. Thouless. Ordering, metastability and phase transitions in two-dimensional systems. *Journal of Physics C: Solid State Physics*, 6(7):1181, 1973. <http://stacks.iop.org/0022-3719/6/i=7/a=010>.
- [6] E. Babaev, L. D. Faddeev, and A. J. Niemi. Hidden symmetry and knot solitons in a charged two-condensate Bose system. *Phys. Rev. B*, 65:100512, Feb 2002. <https://link.aps.org/doi/10.1103/PhysRevB.65.100512>.
- [7] E. Babaev. Vortices with Fractional Flux in Two-Gap Superconductors and in Extended Faddeev Model. *Phys. Rev. Lett.*, 89:067001, Jul 2002. <https://link.aps.org/doi/10.1103/PhysRevLett.89.067001>.
- [8] J. Garaud, K. A. H. Sellin, J. Jäykkä, and E. Babaev. Skyrmions induced by dissipationless drag in  $U(1) \times U(1)$  superconductors. *Phys. Rev. B*, 89:104508, Mar 2014. <https://link.aps.org/doi/10.1103/PhysRevB.89.104508>.

- [9] D. F. Agterberg. Square vortex lattices for two-component superconducting order parameters. *Phys. Rev. B*, 58:14484–14489, Dec 1998. <https://link.aps.org/doi/10.1103/PhysRevB.58.14484>.
- [10] E. Babaev and M. Speight. Semi-Meissner state and neither type-I nor type-II superconductivity in multicomponent superconductors. *Physical Review B*, 72(18):180502, 2005. <https://doi.org/10.1103/PhysRevB.72.180502>.
- [11] W. H. Keesom and A. P. Keesom. New measurements on the specific heat of liquid helium. *Physica*, 2(1):557 – 572, 1935. <http://www.sciencedirect.com/science/article/pii/S0031891435901288>.
- [12] L. Onsager. *Nuovo Cimento (Supplemento)*, 6:249, 1949.
- [13] M. E. Peskin. Mandelstam-'t Hooft duality in abelian lattice models. *Annals of Physics*, 113(1):122 – 152, 1978. <http://www.sciencedirect.com/science/article/pii/000349167890252X>.
- [14] C. Dasgupta and B. Halperin. Phase Transition in a Lattice Model of Superconductivity. *Phys. Rev. Lett.*, 47:1556–1560, Nov 1981. <http://link.aps.org/doi/10.1103/PhysRevLett.47.1556>.
- [15] A. Kuklov, N. Prokof'ev, and B. Svistunov. Ginzburg-Landau-Wilson Aspect of Deconfined Criticality. *arXiv:cond-mat/0501052*, January 2005. <https://arxiv.org/abs/cond-mat/0501052>.
- [16] A. B. Kuklov, N. V. Prokof'ev, B. V. Svistunov, and M. Troyer. Deconfined criticality, runaway flow in the two-component scalar electrodynamics and weak first-order superfluid-solid transitions . *Annals of Physics*, 321(7):1602 – 1621, 2006. <http://www.sciencedirect.com/science/article/pii/S0003491606000789>.
- [17] E. Dahl, E. Babaev, S. Kragset, and A. Sudbø. Preemptive vortex-loop proliferation in multicomponent interacting Bose-Einstein condensates. *Phys. Rev. B*, 77:144519, Apr 2008. <http://link.aps.org/doi/10.1103/PhysRevB.77.144519>.
- [18] E. Herland, E. Babaev, and A. Sudbø. Phase transitions in a three dimensional  $U(1) \times U(1)$  lattice London superconductor: Metallic superfluid and charge- $4e$  superconducting states. *Phys. Rev. B*, 82:134511, Oct 2010. <http://link.aps.org/doi/10.1103/PhysRevB.82.134511>.
- [19] H. K. Onnes. *Further experiments with Liquid Helium. G. On the Electrical Resistance of Pure Metals, etc. VI. On the Sudden Change in the Rate at which the Resistance of Mercury Disappears.*, pages 267–272.

- Springer Netherlands, Dordrecht, 1991. [https://doi.org/10.1007/978-94-009-2079-8\\_17](https://doi.org/10.1007/978-94-009-2079-8_17).
- [20] W. Meissner and R. Ochsenfeld. Ein neuer Effekt bei Eintritt der Supraleitfähigkeit. *Naturwissenschaften*, 21(44):787–788, 1933. <http://dx.doi.org/10.1007/BF01504252>.
  - [21] R. P. Feynman. Superfluidity and Superconductivity. *Rev. Mod. Phys.*, 29:205–212, Apr 1957. <https://link.aps.org/doi/10.1103/RevModPhys.29.205>.
  - [22] J. Bardeen, L. N. Cooper, and J. R. Schrieffer. Theory of Superconductivity. *Phys. Rev.*, 108:1175–1204, Dec 1957. <http://link.aps.org/doi/10.1103/PhysRev.108.1175>.
  - [23] E. M. Lifshitz and L. P. Pitaevskii. *Statistical Physics Part 2*, volume 9 of *Landau and Lifshitz Course of Theoretical Physics*. Pergamon Press, 1980.
  - [24] L. P. Gorkov. Microscopic derivation of the Ginzburg-Landau equations in the theory of superconductivity. *Soviet Physics JETP*, 9(6):1364–1367, 1959. <http://www.jetp.ac.ru/cgi-bin/e/index/e/9/6/p1364?a=list>.
  - [25] M. Tinkham. *Introduction to superconductivity*. Dover Publications, Inc., 2nd edition, 2004.
  - [26] N. E. Phillips. Heat Capacity of Aluminum between 0.1°K and 4.0°K. *Phys. Rev.*, 114:676–685, May 1959. <https://link.aps.org/doi/10.1103/PhysRev.114.676>.
  - [27] F. London. *Superfluids Volume 2*. Structure of Matter Series. John Wiley & Sons, Inc., 1954.
  - [28] R. F. Shiozaki, G. D. Telles, P. Castilho, F. J. Poveda-Cuevas, S. R. Muniz, G. Roati, V. Romero-Rochin, and V. S. Bagnato. Measuring the heat capacity in a Bose-Einstein condensation using global variables. *Phys. Rev. A*, 90:043640, Oct 2014. <https://link.aps.org/doi/10.1103/PhysRevA.90.043640>.
  - [29] V. Moshchalkov, M. Menghini, T. Nishio, Q. H. Chen, A. V. Silhanek, V. H. Dao, L. F. Chibotaru, N. D. Zhigadlo, and J. Karpinski. Type-1.5 Superconductivity. *Phys. Rev. Lett.*, 102:117001, Mar 2009. <https://link.aps.org/doi/10.1103/PhysRevLett.102.117001>.
  - [30] T. Nishio, V. H. Dao, Q. Chen, L. F. Chibotaru, K. Kadowaki, and V. V. Moshchalkov. Scanning SQUID microscopy of vortex clusters in multiband superconductors. *Phys. Rev. B*, 81:020506, Jan 2010. <https://link.aps.org/doi/10.1103/PhysRevB.81.020506>.

- [31] E. Babaev, J. Carlström, and M. Speight. Type-1.5 Superconducting State from an Intrinsic Proximity Effect in Two-Band Superconductors. *Phys. Rev. Lett.*, 105:067003, Aug 2010. <https://link.aps.org/doi/10.1103/PhysRevLett.105.067003>.
- [32] M. Silaev and E. Babaev. Microscopic theory of type-1.5 superconductivity in multiband systems. *Phys. Rev. B*, 84:094515, Sep 2011. <https://link.aps.org/doi/10.1103/PhysRevB.84.094515>.
- [33] V. H. Dao, L. F. Chibotaru, T. Nishio, and V. V. Moshchalkov. Giant vortices, rings of vortices, and reentrant behavior in type-1.5 superconductors. *Phys. Rev. B*, 83:020503, Jan 2011. <https://link.aps.org/doi/10.1103/PhysRevB.83.020503>.
- [34] J. Carlström, J. Garaud, and E. Babaev. Semi-Meissner state and nonpairwise intervortex interactions in type-1.5 superconductors. *Phys. Rev. B*, 84:134515, Oct 2011. <https://link.aps.org/doi/10.1103/PhysRevB.84.134515>.
- [35] J. Carlström, J. Garaud, and E. Babaev. Length scales, collective modes, and type-1.5 regimes in three-band superconductors. *Phys. Rev. B*, 84:134518, Oct 2011. <https://link.aps.org/doi/10.1103/PhysRevB.84.134518>.
- [36] J. Carlström, E. Babaev, and M. Speight. Type-1.5 superconductivity in multiband systems: Effects of interband couplings. *Phys. Rev. B*, 83:174509, May 2011. <https://link.aps.org/doi/10.1103/PhysRevB.83.174509>.
- [37] J. Garaud, D. F. Agterberg, and E. Babaev. Vortex coalescence and type-1.5 superconductivity in  $\text{Sr}_2\text{RuO}_4$ . *Phys. Rev. B*, 86:060513, Aug 2012. <https://link.aps.org/doi/10.1103/PhysRevB.86.060513>.
- [38] J. Gutierrez, B. Raes, A. V. Silhanek, L. J. Li, N. D. Zhigadlo, J. Karpinski, J. Tempere, and V. V. Moshchalkov. Scanning Hall probe microscopy of unconventional vortex patterns in the two-gap  $\text{MgB}_2$  superconductor. *Phys. Rev. B*, 85:094511, Mar 2012. <https://link.aps.org/doi/10.1103/PhysRevB.85.094511>.
- [39] S. J. Ray, A. S. Gibbs, S. J. Bending, P. J. Curran, E. Babaev, C. Baines, A. P. Mackenzie, and S. L. Lee. Muon-spin rotation measurements of the vortex state in  $\text{Sr}_2\text{RuO}_4$ : Type-1.5 superconductivity, vortex clustering, and a crossover from a triangular to a square vortex lattice. *Phys. Rev. B*, 89:094504, Mar 2014. <https://link.aps.org/doi/10.1103/PhysRevB.89.094504>.

- [40] A. Edström. Three and four-body intervortex forces in the Ginzburg-Landau models of single- and multicomponent superconductivity. *Physica C: Superconductivity*, 487(Supplement C):19 – 26, 2013. <http://www.sciencedirect.com/science/article/pii/S0921453413000233>.
- [41] J. Garaud and E. Babaev. Vortex chains due to nonpairwise interactions and field-induced phase transitions between states with different broken symmetry in superconductors with competing order parameters. *Phys. Rev. B*, 91:014510, Jan 2015. <http://link.aps.org/doi/10.1103/PhysRevB.91.014510>.
- [42] R. Díaz-Méndez, F. Mezzacapo, W. Lechner, F. Cinti, E. Babaev, and G. Pupillo. Glass Transitions in Monodisperse Cluster-Forming Ensembles: Vortex Matter in Type-1.5 Superconductors. *Phys. Rev. Lett.*, 118:067001, Feb 2017. <https://link.aps.org/doi/10.1103/PhysRevLett.118.067001>.
- [43] N. D. Mermin and H. Wagner. Absence of Ferromagnetism or Antiferromagnetism in One- or Two-Dimensional Isotropic Heisenberg Models. *Phys. Rev. Lett.*, 17:1133–1136, Nov 1966. <https://link.aps.org/doi/10.1103/PhysRevLett.17.1133>.
- [44] J. M. Kosterlitz. The critical properties of the two-dimensional xy model. *Journal of Physics C: Solid State Physics*, 7(6):1046, 1974. <http://stacks.iop.org/0022-3719/7/i=6/a=005>.
- [45] B. I. Halperin and D. R. Nelson. Resistive transition in superconducting films. *Journal of Low Temperature Physics*, 36(5):599–616, Sep 1979. <https://doi.org/10.1007/BF00116988>.
- [46] D. J. Bishop and J. D. Reppy. Study of the Superfluid Transition in Two-Dimensional  $^4\text{He}$  Films. *Phys. Rev. Lett.*, 40:1727–1730, Jun 1978. <https://link.aps.org/doi/10.1103/PhysRevLett.40.1727>.
- [47] A. F. Hebard and A. T. Fiory. Evidence for the Kosterlitz-Thouless Transition in Thin Superconducting Aluminum Films. *Phys. Rev. Lett.*, 44:291–294, Jan 1980. <https://link.aps.org/doi/10.1103/PhysRevLett.44.291>.
- [48] K. Epstein, A. M. Goldman, and A. M. Kadin. Vortex-Antivortex Pair Dissociation in Two-Dimensional Superconductors. *Phys. Rev. Lett.*, 47:534–537, Aug 1981. <https://link.aps.org/doi/10.1103/PhysRevLett.47.534>.
- [49] A. K. Nguyen and A. Sudbø. Onsager loop transition and first-order flux-line lattice melting in high- $T_c$  superconductors. *Phys. Rev.*

- B*, 57:3123–3143, Feb 1998. <https://link.aps.org/doi/10.1103/PhysRevB.57.3123>.
- [50] K. Fossheim and A. Sudbø. *Superconductivity: Physics and Applications*. John Wiley & Sons, 2004.
  - [51] B. Svistunov, E. Babaev, and N. Prokof'ev. *Superfluid States of Matter*. CRC Press, 2015.
  - [52] A. Brown, M. W. Zemansky, and H. A. Boorse. The Superconducting and Normal Heat Capacities of Niobium. *Phys. Rev.*, 92:52–58, Oct 1953. <http://link.aps.org/doi/10.1103/PhysRev.92.52>.
  - [53] B. I. Halperin, T. C. Lubensky, and S. Ma. First-Order Phase Transitions in Superconductors and Smectic-*A* Liquid Crystals. *Phys. Rev. Lett.*, 32:292–295, Feb 1974. <http://link.aps.org/doi/10.1103/PhysRevLett.32.292>.
  - [54] H. Kleinert. Disorder version of the Abelian Higgs model and the order of the superconductive phase transition. *Lettere al Nuovo Cimento (1971-1985)*, 35(13):405–412, Nov 1982. <https://doi.org/10.1007/BF02754760>.
  - [55] J. Bartholomew. Phase structure of a lattice superconductor. *Phys. Rev. B*, 28:5378–5381, Nov 1983. <http://link.aps.org/doi/10.1103/PhysRevB.28.5378>.
  - [56] I. F. Herbut and Z. Tešanović. Critical Fluctuations in Superconductors and the Magnetic Field Penetration Depth. *Phys. Rev. Lett.*, 76:4588–4591, Jun 1996. <http://link.aps.org/doi/10.1103/PhysRevLett.76.4588>.
  - [57] S. Mo, J. Hove, and A. Sudbø. Order of the metal-to-superconductor transition. *Phys. Rev. B*, 65:104501, Jan 2002. <http://link.aps.org/doi/10.1103/PhysRevB.65.104501>.
  - [58] G. Fejős and T. Hatsuda. Fixed point structure of the Abelian Higgs model. *Phys. Rev. D*, 93:121701, Jun 2016. <https://link.aps.org/doi/10.1103/PhysRevD.93.121701>.
  - [59] G. Fejős and T. Hatsuda. Renormalization group flows of the  $N$ -component Abelian Higgs model. *Phys. Rev. D*, 96:056018, Sep 2017. <https://link.aps.org/doi/10.1103/PhysRevD.96.056018>.
  - [60] J. F. Annett. *Superconductivity, Superfluids and Condensates*, volume 5 of *Oxford Master Series in Physics*. Oxford University Press, 2004.

- [61] J. A. Lipa, D. R. Swanson, J. A. Nissen, T. C. P. Chui, and U. E. Israelsson. Heat Capacity and Thermal Relaxation of Bulk Helium very near the Lambda Point. *Phys. Rev. Lett.*, 76:944–947, Feb 1996. <https://link.aps.org/doi/10.1103/PhysRevLett.76.944>.
- [62] J. A. Lipa, J. A. Nissen, D. A. Stricker, D. R. Swanson, and T. C. P. Chui. Specific heat of liquid helium in zero gravity very near the lambda point. *Phys. Rev. B*, 68:174518, Nov 2003. <https://link.aps.org/doi/10.1103/PhysRevB.68.174518>.
- [63] J. Lidmar, M. Wallin, C. Wengel, S. M. Girvin, and A. P. Young. Dynamical universality classes of the superconducting phase transition. *Phys. Rev. B*, 58:2827–2833, Aug 1998. <https://link.aps.org/doi/10.1103/PhysRevB.58.2827>.
- [64] P. Olsson and S. Teitel. Critical Behavior of the Meissner Transition in the Lattice London Superconductor. *Phys. Rev. Lett.*, 80:1964–1967, Mar 1998. <http://link.aps.org/doi/10.1103/PhysRevLett.80.1964>.
- [65] P. Olsson. Critical exponent  $\eta_\phi$  of the lattice London superconductor and vortex loops in the 3D XY model. *EPL (Europhysics Letters)*, 58(5):705, 2002. <http://stacks.iop.org/0295-5075/58/i=5/a=705>.
- [66] T. Neuhaus, A. Rajantie, and K. Rummukainen. The inverted XY universality of the superconductivity phase transition. *Nuclear Physics B - Proceedings Supplements*, 119(Supplement C):915 – 917, 2003. <http://www.sciencedirect.com/science/article/pii/S0920563203804851>.
- [67] H. Meier, E. Babaev, and M. Wallin. Fluctuation-induced first-order phase transitions in type-1.5 superconductors in zero external field. *Phys. Rev. B*, 91:094508, Mar 2015. <http://link.aps.org/doi/10.1103/PhysRevB.91.094508>.
- [68] C. T. Lane. *Superfluid Physics*. McGraw-Hill Book Company, Inc., 1962.
- [69] R. P. Feynman. *Statistical Mechanics: A Set Of Lectures*. Advanced Books Program. W. A. Benjamin, Inc., 1972.
- [70] F. London. On the Bose-Einstein Condensation. *Phys. Rev.*, 54:947–954, Dec 1938. <https://link.aps.org/doi/10.1103/PhysRev.54.947>.
- [71] S. R. De Groot, G. J. Hooyman, and C. A. Ten Seldam. On the Bose-Einstein condensation. *Proceedings of the Royal Society of London A: Mathematical, Physical and Engineering Sciences*, 203(1073):266–286, 1950. <http://rspa.royalsocietypublishing.org/content/203/1073/266>.

- [72] V. Bagnato, D. E. Pritchard, and D. Kleppner. Bose-Einstein condensation in an external potential. *Phys. Rev. A*, 35:4354–4358, May 1987. <https://link.aps.org/doi/10.1103/PhysRevA.35.4354>.
- [73] S. Grossmann and M. Holthaus. On Bose-Einstein condensation in harmonic traps. *Physics Letters A*, 208(3):188 – 192, 1995. <http://www.sciencedirect.com/science/article/pii/037596019500766V>.
- [74] R. P. Feynman. Atomic Theory of the  $\lambda$  Transition in Helium. *Phys. Rev.*, 91:1291–1301, Sep 1953. <https://link.aps.org/doi/10.1103/PhysRev.91.1291>.
- [75] D. M. Ceperley and E. L. Pollock. Path-integral computation of the low-temperature properties of liquid  $^4\text{He}$ . *Phys. Rev. Lett.*, 56:351–354, Jan 1986. <https://link.aps.org/doi/10.1103/PhysRevLett.56.351>.
- [76] D. M. Ceperley. Path integrals in the theory of condensed helium. *Rev. Mod. Phys.*, 67:279–355, Apr 1995. <https://link.aps.org/doi/10.1103/RevModPhys.67.279>.
- [77] E. L. Pollock and D. M. Ceperley. Path-integral computation of superfluid densities. *Phys. Rev. B*, 36:8343–8352, Dec 1987. <https://link.aps.org/doi/10.1103/PhysRevB.36.8343>.
- [78] N. V. Prokof'ev, B. V. Svistunov, and I. S. Tupitsyn. “Worm” algorithm in quantum Monte Carlo simulations. *Physics Letters A*, 238(4):253 – 257, Feb 1998. <http://www.sciencedirect.com/science/article/pii/S0375960197009572>.
- [79] N. V. Prokof'ev, B. V. Svistunov, and I. S. Tupitsyn. Exact, complete, and universal continuous-time worldline Monte Carlo approach to the statistics of discrete quantum systems. *Journal of Experimental and Theoretical Physics*, 87(2):310–321, Aug 1998. <https://doi.org/10.1134/1.558661>.
- [80] M. Boninsegni, N. Prokof'ev, and B. Svistunov. Worm Algorithm for Continuous-Space Path Integral Monte Carlo Simulations. *Phys. Rev. Lett.*, 96:070601, Feb 2006. <https://link.aps.org/doi/10.1103/PhysRevLett.96.070601>.
- [81] M. Boninsegni, N. V. Prokof'ev, and B. V. Svistunov. Worm algorithm and diagrammatic Monte Carlo: A new approach to continuous-space path integral Monte Carlo simulations. *Phys. Rev. E*, 74:036701, Sep 2006. <https://link.aps.org/doi/10.1103/PhysRevE.74.036701>.

- [82] R. J. Baxter. *Exactly Solved Models in Statistical Mechanics*. Academic Press, 1989.
- [83] N. Metropolis, A. W. Rosenbluth, M. N. Rosenbluth, A. H. Teller, and E. Teller. Equation of State Calculations by Fast Computing Machines. *The Journal of Chemical Physics*, 21(6):1087–1092, 1953. <http://scitation.aip.org/content/aip/journal/jcp/21/6/10.1063/1.1699114>.
- [84] D. W. Heermann. *Computer Simulation Methods in Theoretical Physics*. Springer-Verlag New York Berlin Heidelberg, 2nd edition, 1990.
- [85] V. Dumoulin and F. Thouin. A Ballistic Monte Carlo Approximation of  $\pi$ , 2014. <https://arxiv.org/abs/1404.1499>.
- [86] M. E. J. Newman and G. T. Barkema. *Monte Carlo Methods in Statistical Physics*. Clarendon Press, 1999.
- [87] D. P. Landau and K. Binder. *A Guide to Monte Carlo Simulations in Statistical Physics*. Cambridge University Press, 4th edition, 2014.
- [88] V. I. Manousiouthakis and M. W. Deem. Strict detailed balance is unnecessary in Monte Carlo simulation. *The Journal of Chemical Physics*, 110(6):2753–2756, 1999. <http://scitation.aip.org/content/aip/journal/jcp/110/6/10.1063/1.477973>.
- [89] M. S. S. Challa, D. P. Landau, and K. Binder. Finite-size effects at temperature-driven first-order transitions. *Phys. Rev. B*, 34:1841–1852, Aug 1986. <http://link.aps.org/doi/10.1103/PhysRevB.34.1841>.
- [90] J. Lee and J. Kosterlitz. New numerical method to study phase transitions. *Phys. Rev. Lett.*, 65:137–140, Jul 1990. <http://link.aps.org/doi/10.1103/PhysRevLett.65.137>.
- [91] J. Lee and J. Kosterlitz. Finite-size scaling and Monte Carlo simulations of first-order phase transitions. *Phys. Rev. B*, 43:3265–3277, Feb 1991. <http://link.aps.org/doi/10.1103/PhysRevB.43.3265>.
- [92] R. H. Swendsen and J. Wang. Replica Monte Carlo Simulation of Spin-Glasses. *Phys. Rev. Lett.*, 57:2607–2609, Nov 1986. <http://link.aps.org/doi/10.1103/PhysRevLett.57.2607>.
- [93] D. J. Earl and M. W. Deem. Parallel tempering: Theory, applications, and new perspectives. *Phys. Chem. Chem. Phys.*, 7:3910–3916, 2005. <http://dx.doi.org/10.1039/B509983H>.

- [94] D. Ruelle. *Statistical Mechanics: Rigorous results*. World Scientific, 1999.
- [95] N. Goldenfeld. *Lectures on phase transitions and the renormalization group*. Frontiers in physics. Perseus Books, 1992.
- [96] P. Ehrenfest. Phasenumwandlungen im ueblichen und erweiterten Sinn, classifiziert nach den entsprechenden Singularitaeten des thermodynamischen Potentialaes. NV Noord-Hollandsche Uitgevers Maatschappij, 1933. Translated version by T. Sauer. Eur. Phys. J. Spec. Top. (2017) 226: 539. <https://doi.org/10.1140/epjst/e2016-60344-y>.
- [97] A. B. Pippard. *Elements of classical thermodynamics: for advanced students of physics*. Cambridge University Press, 1964.
- [98] M. E. Fisher. The theory of equilibrium critical phenomena. *Reports on progress in physics*, 30(2):615, 1967. <https://doi.org/10.1088/0034-4885/30/2/306>.
- [99] G. Jaeger. The Ehrenfest classification of phase transitions: introduction and evolution. *Archive for history of exact sciences*, 53(1):51–81, 1998. <https://doi.org/10.1007/s004070050021>.
- [100] U. Essmann and H. Träuble. The direct observation of individual flux lines in type II superconductors. *Physics Letters A*, 24(10):526 – 527, 1967. <http://www.sciencedirect.com/science/article/pii/0375960167908195>.
- [101] P. L. Gammel, D. J. Bishop, G. J. Dolan, J. R. Kwo, C. A. Murray, L. F. Schneemeyer, and J. V. Waszczak. Observation of Hexagonally Correlated Flux Quanta In  $\text{YBa}_2\text{Cu}_3\text{O}_7$ . *Phys. Rev. Lett.*, 59:2592–2595, Nov 1987. <https://link.aps.org/doi/10.1103/PhysRevLett.59.2592>.
- [102] H. F. Hess, R. B. Robinson, R. C. Dynes, J. M. Valles, and J. V. Waszczak. Scanning-Tunneling-Microscope Observation of the Abrikosov Flux Lattice and the Density of States near and inside a Fluxoid. *Phys. Rev. Lett.*, 62:214–216, Jan 1989. <https://link.aps.org/doi/10.1103/PhysRevLett.62.214>.
- [103] L. Y. Vinnikov, J. Karpinski, S. M. Kazakov, J. Jun, J. Anderegg, S. L. Bud'ko, and P. C. Canfield. Vortex structure in  $\text{MgB}_2$  single crystals observed by the Bitter decoration technique. *Phys. Rev. B*, 67:092512, Mar 2003. <http://link.aps.org/doi/10.1103/PhysRevB.67.092512>.

- [104] H. Yang, B. Shen, Z. Wang, L. Shan, C. Ren, and H. Wen. Vortex images on  $\text{Ba}_{1-x}\text{K}_x\text{Fe}_2\text{As}_2$  observed directly by magnetic force microscopy. *Phys. Rev. B*, 85:014524, Jan 2012. <http://link.aps.org/doi/10.1103/PhysRevB.85.014524>.
- [105] L. J. Li, T. Nishio, Z. A. Xu, and V. V. Moshchalkov. Low-field vortex patterns in the multiband  $\text{BaFe}_{2-x}\text{Ni}_x\text{As}_2$  superconductor ( $x = 0.1, 0.16$ ). *Phys. Rev. B*, 83:224522, Jun 2011. <http://link.aps.org/doi/10.1103/PhysRevB.83.224522>.
- [106] O. Romero-Isart, C. Navau, A. Sanchez, P. Zoller, and J. I. Cirac. Superconducting Vortex Lattices for Ultracold Atoms. *Phys. Rev. Lett.*, 111:145304, Oct 2013. <http://link.aps.org/doi/10.1103/PhysRevLett.111.145304>.
- [107] Q. Meng, C. N. Varney, H. Fangohr, and E. Babaev. Honeycomb, square, and kagome vortex lattices in superconducting systems with multiscale intervortex interactions. *Phys. Rev. B*, 90:020509, Jul 2014. <https://link.aps.org/doi/10.1103/PhysRevB.90.020509>.
- [108] C. Reichhardt and G. T. Zimányi. Melting of moving vortex lattices in systems with periodic pinning. *Phys. Rev. B*, 61:14354–14357, Jun 2000. <http://link.aps.org/doi/10.1103/PhysRevB.61.14354>.
- [109] H. Fangohr, S. J. Cox, and P. A. J. de Groot. Vortex dynamics in two-dimensional systems at high driving forces. *Phys. Rev. B*, 64:064505, Jul 2001. <https://link.aps.org/doi/10.1103/PhysRevB.64.064505>.
- [110] C. J. Olson Reichhardt, C. Reichhardt, and A. R. Bishop. Structural transitions, melting, and intermediate phases for stripe- and clump-forming systems. *Phys. Rev. E*, 82:041502, Oct 2010. <http://link.aps.org/doi/10.1103/PhysRevE.82.041502>.
- [111] A. F. Andreev and E. P. Bashkin. Three-velocity hydrodynamics of superfluid solutions. *Soviet Physics JETP*, 42(1):164–167, 1975. <http://www.jetp.ac.ru/cgi-bin/e/index/e/42/1/p164?a=list>.
- [112] B. M. A. G. Piette, B. J. Schroers, and W. J. Zakrzewski. Multisolitons in a two-dimensional Skyrme model. *Zeitschrift für Physik C Particles and Fields*, 65(1):165–174, 1995. <http://dx.doi.org/10.1007/BF01571317>.
- [113] N. Nagaosa and Y. Tokura. Topological properties and dynamics of magnetic skyrmions. *Nature nanotechnology*, 8(12):899–911, 2013. <http://dx.doi.org/10.1038/nnano.2013.243>.

- [114] M. A. Miller, L. M. Amon, and W. P. Reinhardt. Should one adjust the maximum step size in a Metropolis Monte Carlo simulation? *Chemical Physics Letters*, 331(2):278 – 284, 2000. <http://www.sciencedirect.com/science/article/pii/S0009261400012173>.
- [115] R. H. Swendsen. How the maximum step size in Monte Carlo simulations should be adjusted. *Physics Procedia*, 15(Supplement C):81 – 86, 2011. <http://www.sciencedirect.com/science/article/pii/S187538921100335X>.
- [116] D. R. Tilley. The Ginzburg-Landau equations for pure two band superconductors. *Proceedings of the Physical Society*, 84(4):573, 1964. <http://stacks.iop.org/0370-1328/84/i=4/a=313>.
- [117] M. Silaev and E. Babaev. Microscopic derivation of two-component Ginzburg-Landau model and conditions of its applicability in two-band systems. *Phys. Rev. B*, 85:134514, Apr 2012. <http://link.aps.org/doi/10.1103/PhysRevB.85.134514>.
- [118] E. Smørgrav, E. Babaev, J. Smiseth, and A. Sudbø. Observation of a Metallic Superfluid in a Numerical Experiment. *Phys. Rev. Lett.*, 95:135301, Sep 2005. <https://link.aps.org/doi/10.1103/PhysRevLett.95.135301>.
- [119] M. H. Anderson, J. R. Ensher, M. R. Matthews, C. E. Wieman, and E. A. Cornell. Observation of Bose-Einstein Condensation in a Dilute Atomic Vapor. *Science*, 269(5221):198–201, 1995. <http://science.sciencemag.org/content/269/5221/198>.
- [120] K. B. Davis, M. Mewes, M. R. Andrews, N. J. van Druten, D. S. Durfee, D. M. Kurn, and W. Ketterle. Bose-Einstein Condensation in a Gas of Sodium Atoms. *Phys. Rev. Lett.*, 75:3969–3973, Nov 1995. <https://link.aps.org/doi/10.1103/PhysRevLett.75.3969>.
- [121] D. Jaksch, C. Bruder, J. I. Cirac, C. W. Gardiner, and P. Zoller. Cold Bosonic Atoms in Optical Lattices. *Phys. Rev. Lett.*, 81:3108–3111, Oct 1998. <https://link.aps.org/doi/10.1103/PhysRevLett.81.3108>.
- [122] M. Greiner, O. Mandel, T. Esslinger, T. W. Hänsch, and I. Bloch. Quantum phase transition from a superfluid to a Mott insulator in a gas of ultracold atoms. *Nature*, 415(6867):39–44, 2002. <http://dx.doi.org/10.1038/415039a>.
- [123] W. S. Bakr, A. Peng, M. E. Tai, R. Ma, J. Simon, J. I. Gillen, S. Fölling, L. Pollet, and M. Greiner. Probing the Superfluid-to-Mott Insulator Transition at the Single-Atom Level. *Science*, 329(5991):547–550, 2010. <http://science.sciencemag.org/content/329/5991/547>.

- [124] H. A. Gersch and G. C. Knollman. Quantum cell model for bosons. *Phys. Rev.*, 129:959–967, Jan 1963. <https://link.aps.org/doi/10.1103/PhysRev.129.959>.
- [125] M. P. A. Fisher, P. B. Weichman, G. Grinstein, and D. S. Fisher. Boson localization and the superfluid-insulator transition. *Phys. Rev. B*, 40:546–570, Jul 1989. <https://link.aps.org/doi/10.1103/PhysRevB.40.546>.
- [126] I. Herbut. *A modern approach to critical phenomena*. Cambridge University Press, 2007.
- [127] G. G. Batrouni and R. T. Scalettar. World-line quantum Monte Carlo algorithm for a one-dimensional Bose model. *Phys. Rev. B*, 46:9051–9062, Oct 1992. <https://link.aps.org/doi/10.1103/PhysRevB.46.9051>.
- [128] B. Capogrosso-Sansone, S. G. Söyler, N. Prokof'ev, and B. Svistunov. Monte Carlo study of the two-dimensional Bose-Hubbard model. *Phys. Rev. A*, 77:015602, Jan 2008. <https://link.aps.org/doi/10.1103/PhysRevA.77.015602>.
- [129] B. Capogrosso-Sansone, N. V. Prokof'ev, and B. V. Svistunov. Phase diagram and thermodynamics of the three-dimensional Bose-Hubbard model. *Phys. Rev. B*, 75:134302, Apr 2007. <https://link.aps.org/doi/10.1103/PhysRevB.75.134302>.
- [130] S. Ejima, H. Fehske, F. Gebhard, K. zu Münster, M. Knap, E. Arigoni, and W. von der Linden. Characterization of Mott-insulating and superfluid phases in the one-dimensional Bose-Hubbard model. *Phys. Rev. A*, 85:053644, May 2012. <https://link.aps.org/doi/10.1103/PhysRevA.85.053644>.
- [131] B. Damski and J. Zakrzewski. Mott-insulator phase of the one-dimensional Bose-Hubbard model: A high-order perturbative study. *Phys. Rev. A*, 74:043609, Oct 2006. <https://link.aps.org/doi/10.1103/PhysRevA.74.043609>.
- [132] R. P. Feynman. Atomic Theory of the  $\lambda$  Transition in Helium. *Phys. Rev.*, 91:1291–1301, Sep 1953. <http://link.aps.org/doi/10.1103/PhysRev.91.1291>.
- [133] R. P. Feynman and A. R. Hibbs. *Quantum Mechanics and Path Integrals*. Dover Publications Inc., emended edition, 2005.
- [134] A. L. Fetter and J. D. Walecka. *Quantum theory of many-particle systems*. Dover Publications, Inc., 2003.

- [135] M. Troyer, F. Alet, S. Trebst, and S. Wessel. Non-local Updates for Quantum Monte Carlo Simulations. *AIP Conference Proceedings*, 690(1):156–169, 2003. <http://aip.scitation.org/doi/abs/10.1063/1.1632126>.
- [136] L. Pollet, K. Van Houcke, and S. M. Rombouts. Engineering local optimality in quantum Monte Carlo algorithms. *Journal of Computational Physics*, 225(2):2249 – 2266, 2007. <http://dx.doi.org/10.1016/j.jcp.2007.03.013>.
- [137] L. Pollet. Recent developments in quantum Monte Carlo simulations with applications for cold gases. *Reports on Progress in Physics*, 75(9):094501, 2012. <http://stacks.iop.org/0034-4885/75/i=9/a=094501>.
- [138] R. P. Feynman. Space-Time Approach to Non-Relativistic Quantum Mechanics. *Rev. Mod. Phys.*, 20:367–387, Apr 1948. <https://link.aps.org/doi/10.1103/RevModPhys.20.367>.
- [139] E. Y. Loh, J. E. Gubernatis, R. T. Scalettar, S. R. White, D. J. Scalapino, and R. L. Sugar. Sign problem in the numerical simulation of many-electron systems. *Phys. Rev. B*, 41:9301–9307, May 1990. <https://link.aps.org/doi/10.1103/PhysRevB.41.9301>.
- [140] M. Troyer and U. Wiese. Computational Complexity and Fundamental Limitations to Fermionic Quantum Monte Carlo Simulations. *Phys. Rev. Lett.*, 94:170201, May 2005. <https://link.aps.org/doi/10.1103/PhysRevLett.94.170201>.
- [141] N. Prokof'ev and B. Svistunov. Bold Diagrammatic Monte Carlo Technique: When the Sign Problem Is Welcome. *Phys. Rev. Lett.*, 99:250201, Dec 2007. <https://link.aps.org/doi/10.1103/PhysRevLett.99.250201>.
- [142] N. V. Prokof'ev and B. V. Svistunov. Bold diagrammatic Monte Carlo: A generic sign-problem tolerant technique for polaron models and possibly interacting many-body problems. *Phys. Rev. B*, 77:125101, Mar 2008. <https://link.aps.org/doi/10.1103/PhysRevB.77.125101>.
- [143] E. Kozik, K. V. Houcke, E. Gull, L. Pollet, N. Prokof'ev, B. Svistunov, and M. Troyer. Diagrammatic Monte Carlo for correlated fermions. *EPL (Europhysics Letters)*, 90(1):10004, 2010. <http://stacks.iop.org/0295-5075/90/i=1/a=10004>.
- [144] K. V. Houcke, E. Kozik, N. Prokof'ev, and B. Svistunov. Diagrammatic Monte Carlo. *Physics Procedia*, 6(Supplement C):95 – 105, 2010. <http://www.sciencedirect.com/science/article/pii/S1875389210006498>.

- [145] K. Van Houcke, F. Werner, E. Kozik, N. Prokofev, B. Svistunov, M. Ku, A. Sommer, L. Cheuk, A. Schirozek, and M. Zwierlein. Feynman diagrams versus Fermi-gas Feynman emulator. *Nature Physics*, 8:366, 2012. <https://doi.org/10.1038/NPHYS2273>.
- [146] I. Bloch, J. Dalibard, and S. Nascimbene. Quantum simulations with ultracold quantum gases. *Nature Physics*, 8(4):267–276, 2012. <https://doi.org/10.1038/NPHYS2259>.
- [147] G. Carleo and M. Troyer. Solving the quantum many-body problem with artificial neural networks. *Science*, 355(6325):602–606, 2017. <http://science.sciencemag.org/content/355/6325/602>.
- [148] P. Broecker, J. Carrasquilla, R. G. Melko, and S. Trebst. Machine learning quantum phases of matter beyond the fermion sign problem. *Scientific Reports*, 7(8823), 2017. <https://doi.org/10.1038/s41598-017-09098-0>.
- [149] K. Ch'ng, J. Carrasquilla, R. G. Melko, and E. Khatami. Machine Learning Phases of Strongly Correlated Fermions. *Phys. Rev. X*, 7:031038, Aug 2017. <https://link.aps.org/doi/10.1103/PhysRevX.7.031038>.
- [150] J. Carrasquilla and R. G. Melko. Machine learning phases of matter. *Nature Physics*, 13:431–434, 2017. <http://dx.doi.org/10.1038/nphys4035>.
- [151] K. Mills, M. Spanner, and I. Tamblyn. Deep learning and the Schrödinger equation. *Phys. Rev. A*, 96:042113, Oct 2017. <https://link.aps.org/doi/10.1103/PhysRevA.96.042113>.
- [152] H. Saito. Solving the Bose-Hubbard Model with Machine Learning. *Journal of the Physical Society of Japan*, 86(9):093001, 2017. <https://doi.org/10.7566/JPSJ.86.093001>.
- [153] R. P. Feynman. Simulating physics with computers. *International Journal of Theoretical Physics*, 21(6):467–488, Jun 1982. <https://doi.org/10.1007/BF02650179>.

